

Measurements of the H I intensity mapping power spectrum at low redshifts with MIGHTEE data: comparison with detected H I galaxies

Junaid Townsend,^{1*} Mario G. Santos,^{1,2} Suman Chatterjee,¹ Zhaoting Chen,^{3,4} Sourabh Paul,⁴ Aishrila Mazumder,⁴ Laura Wolz,⁴ Matt J. Jarvis^{1,5} and Bradley S. Frank^{6,7}

¹*Department of Physics and Astronomy, University of the Western Cape, Robert Sobukwe Road, Bellville, 7535, South Africa*

²*South African Radio Astronomy Observatory (SARAO), Cape Town, 7700, South Africa*

³*Institute for Astronomy, The University of Edinburgh, Royal Observatory, Edinburgh EH9 3HJ, UK*

⁴*Jodrell Bank Centre for Astrophysics, Department of Physics and Astronomy, The University of Manchester, Manchester M13 9PL, UK*

⁵*Astrophysics, Department of Physics, University of Oxford, Keble Road, Oxford, OX1 3RH, UK*

⁶*STFC UK Astronomy Technology Centre, Royal Observatory, Edinburgh, Blackford Hill, Edinburgh, EH9 3HJ*

⁷*Department of Astronomy, University of Cape Town, Private Bag X3, Rondebosch 7701, South Africa*

Accepted XXX. Received YYY; in original form ZZZ

ABSTRACT

Line intensity mapping provides a statistical approach to tracing the large-scale distribution of matter in the Universe. We apply the H I intensity mapping technique to interferometric data from the MeerKAT International GHz-Tiered Extragalactic Explorations (MIGHTEE) Survey, analysing 17.5 hours of a single pointing in the COSMOS field, using a 60 MHz sub-band in the frequency range 1332 - 1392 MHz ($0.02 \lesssim z \lesssim 0.07$). Using a delay-spectrum-based estimator, we measure the H I power spectrum on sub-megaparsec scales and compare it directly to the power spectrum inferred from a catalogue of individually detected H I galaxies in the same field. After mitigating low-level broadband contamination through conservative outlier flagging in the three-dimensional power spectrum, cross-correlation of time-split visibilities yields a statistically significant detection on scales $3 \lesssim k \lesssim 20 \text{ Mpc}^{-1}$ with a total signal-to-noise ratio of ~ 13 . Over this range, the power spectra obtained from visibilities and detected galaxies are consistent within uncertainties and have comparable amplitudes of order $10^{-2} - 10^{-1} \text{ mK}^2 \text{ Mpc}^3$. End-to-end validation is performed by propagating detected galaxies through the power spectrum estimator via both direct intensity-field construction and simulated visibilities, demonstrating agreement up to $k \sim 20 \text{ Mpc}^{-1}$, beyond which measurements become noise-dominated. A statistically significant correlation is also observed between the data and the simulated visibilities from the detected H I galaxies, which should be free of systematics. These results provide a self-consistent validation of interferometric H I intensity mapping at low redshift and demonstrate agreement with galaxy-based measurements within the same cosmological volume.

Key words: Cosmology – techniques: interferometric – radio lines: galaxies

1 INTRODUCTION

Intensity mapping (IM) with the 21 cm emission line of neutral hydrogen (H I) has been proposed as a novel technique to explore the cosmological and astrophysical properties of the Universe (Bharadwaj & Sethi 2001; Bharadwaj et al. 2001; Battye et al. 2004; McQuinn et al. 2006; Chang et al. 2008; Wyithe & Loeb 2009; Bull et al. 2015; Santos et al. 2015a; Kovetz et al. 2017). In the era of precision cosmology in which the Cosmic Microwave Background (CMB) from Recombination at $z \sim 1100$ has provided significant insights into our understanding of the Universe (e.g. Planck Collaboration et al. 2020), IM with the 21-cm line would help make this picture more complete with its large area and deep volume coverage capabilities, allowing us to probe substantial portions of the Universe’s cosmic history. In addition to its fast survey speeds, H I IM also provides excellent redshift information since it measures the 21 cm line, with a rest

frame frequency of ~ 1420 MHz, while radio telescopes typically provide sub-MHz frequency resolutions, without the need for special spectroscopic techniques required for optical surveys. Coupled with the abundance of H I throughout the Universe’s cosmic history, IM provides a means of probing cosmological information all the way up to $z \sim 200$ (Santos & Cooray 2006), well into the Dark Ages. As such, it has the means of providing a comprehensive view of the Universe’s evolution from the present day until the first stars and galaxies started forming and even beyond.

First predicted by van de Hulst (1945) and then detected by Ewen & Purcell (1951), this 21 cm emission line arises from the spin-flip transition of the electron within the hydrogen atom, which then emits a photon of energy at a wavelength of about 21 cm. Despite this transition being highly forbidden, we can observe this emission line with radio telescopes sensitive to centimetre-wavelength radiation due to hydrogen being the most abundant form of baryonic matter in the Universe. During the Epoch of Reionisation (EoR), the hydrogen in the intergalactic medium went from neutral to fully ionised due to

* E-mail: junaidtownsend@gmail.com

the ultraviolet photons and X-ray radiation from the first luminous objects, such as stars within early galaxies (Furlanetto et al. 2006). In the post-reionisation Universe, we expect to find most of the H I within so-called damped Lyman-alpha (Ly- α) systems (Pritchard & Loeb 2012; Villaescusa-Navarro et al. 2014; Spinelli et al. 2021a) that provide shielding from those sources that would otherwise potentially ionise all the H I. Due to this, we observe most of the H I after reionisation within galaxies, galaxy groups, and galaxy clusters. This makes it an excellent tracer of the underlying dark matter density field, which gravitationally binds the Baryonic matter and, therefore, the large-scale structure of the Universe and structure formation history across time. IM with H I also allows us to study the gas content of galaxies in the post-reionisation era (Wolz et al. 2017), which serves as the fundamental fuel reservoir for star formation in galaxies (Huang et al. 2012; Maddox et al. 2015). It helps probe galaxy evolution across cosmic time, which can be compared against state-of-the-art H I galaxy simulations such as SIMBA (Davé et al. 2019). These comparisons will enable us to understand better the astrophysics of H I gas and the galaxies or clusters of galaxies that host it.

Measurements of the H I IM signal are done in practice using statistical measurements via the power spectrum, a 2-point Fourier statistic, which tells us how much H I clustering there is on a range of cosmological scales (Peacock 2003; Dodelson 2003). This can be achieved by surveying large volumes of the Universe with radio telescopes sensitive to the 21 cm line emission, making sky maps across frequency, which can be used to calculate the power spectrum statistic in either cross-correlation with other tracers of dark matter, such as galaxy surveys, or in auto-correlation of the H I intensity maps. There have been numerous experiments designed to do H I IM, with some of them having made detections of the H I power spectrum at various epochs in cross-correlation with galaxy surveys (Chang et al. 2010; Masui et al. 2013; Anderson et al. 2018; Wolz et al. 2021; Cunnington et al. 2022; CHIME Collaboration et al. 2023) or provided upper limits on the auto-correlations (Switzer et al. 2013; MeerKLASS Collaboration et al. 2025) (also see Liu & Shaw 2020 for a review). A detection of the H I auto-power spectrum on small scales at redshifts $z \sim 0.32$ and $z \sim 0.44$ has been reported in Paul et al. (2023), based on 96 hours of MeerKAT data on a single-pointing (Mauch et al. 2020). Generally, two experimental configurations exist for H I intensity mapping. These include single-dish and interferometric instruments. In the post-reionisation era ($z < 6$), single-dish experiments focus on probing larger scales ($k \lesssim 0.1 \text{ Mpc}^{-1}$) by rapidly surveying large sky areas with low angular resolution (Santos et al. 2015b), while the interferometric experiments probe smaller, linear to non-linear scales ($k \gtrsim 0.1 \text{ Mpc}^{-1}$) due to tightly-packed baselines between individual antennas that result in better angular resolution (Newburgh et al. 2016; CHIME Collaboration et al. 2022). In this manner, the two survey types are complementary on angular scales, k_{\perp} , while being sensitive to the same range of line-of-sight scales, k_{\parallel} , set by the bandwidth and frequency resolution of the observing instrument (Bull et al. 2015).

A direct detection of the H I intensity mapping power spectrum presents several challenges due to a combination of instrumental systematics and foregrounds several orders of magnitude stronger than the signal (Barry et al. 2016; Spinelli et al. 2021b; Chen et al. 2022). Cross-correlations with external galaxy surveys can confirm the presence of an H I signal but do not guarantee that the measured auto-power spectrum is free from systematics. Residual contamination such as low-level broadband radio frequency interference (RFI) can contribute power to the measurement. While null tests can increase the confidence in a detection, they cannot completely rule

out subtle, undetected systematics. Ultimately, establishing this technique as a robust cosmological probe will require a combination of well-tested data reduction pipelines and multiple, independent measurements.

In this paper, we aim to address these issues by applying our signal extraction methodology to a self-contained test case, where we directly compare the measured intensity mapping power spectrum to that derived from H I galaxies detected in the same field. We use Early Science visibility data from the MeerKAT International GHz-Tiered Extragalactic Explorations (MIGHTEE) Survey (Jarvis et al. 2016), employing the delay-spectrum technique (Morales & Hewitt 2004; Parsons et al. 2012a,b; Thyagarajan et al. 2013; Parsons et al. 2014; Thyagarajan et al. 2015; Paul et al. 2016; Morales et al. 2019) to measure the H I power spectrum on sub-Megaparsec scales at low redshifts. This technique has primarily been applied to studies of the Epoch of Reionisation (EoR), where it has been used to set upper limits on the 21 cm power spectrum with instruments such as PAPER, the Murchison Widefield Array (MWA), and the Hydrogen Epoch of Reionisation Array (HERA) (e.g., Parsons et al. 2012a; Pober et al. 2013; Parsons et al. 2014; Deboer et al. 2017; HERA Collaboration et al. 2022). More recently, applications of this method in the post-EoR regime have shown promising results, employing foreground avoidance and using statistical measures such as spherical and cylindrical power spectra to analyse both simulated and observational data (Paul et al. 2021; Chen et al. 2021, 2022, 2023; Paul et al. 2023; Mazumder et al. 2025). Comparing the intensity mapping power spectrum to the galaxy power spectrum derived from directly-detected H I galaxies in the same MIGHTEE dataset allows us to test the robustness of the intensity mapping approach in a regime where traditional H I galaxy surveys are still feasible, given the relatively low redshift. This comparison further allows us to evaluate whether either the intensity mapping technique or direct detections using radio interferometric data systematically miss part of the H I content and how consistent the two power spectrum measurements are. Our analysis builds upon and tests the methodology developed in Paul et al. (2023). It also serves as a follow-up to the MIGHTEE-COSMOS analysis presented in Mazumder et al. (2025), where data from multiple COSMOS pointings were incoherently combined to obtain upper limits on the H I power spectrum at $z \sim 0.44$. That study was itself a comparative test of the tentative detection reported in Paul et al. (2023). The MIGHTEE survey, leveraging the wide field-of-view and high sensitivity of MeerKAT, is particularly well-suited for these tests, providing a good sample of H I galaxies at low redshifts.

The rest of the paper is structured as follows. Section 2 outlines the data used in this work. Section 3 focuses on the 'delay'-spectrum methodology and pipeline developed to measure the H I power spectrum from the visibility data, while also showcasing the visibility power spectrum results. Section 4 discusses validations employed using a simulated cosmological volume which contains detected H I galaxies from MIGHTEE. Further validations of the power spectrum results using visibilities simulated on these H I detections are discussed in Section 5, followed by the summary and conclusions in Section 6.

Throughout this paper, a flat ($\Omega_k = 0$) Λ CDM cosmology is assumed, with cosmological parameters $[h, \Omega_M, \Omega_b, n_s, \sigma_8] = [0.674, 0.311, 0.049, 0.965, 0.811]$, corresponding with those from the latest Planck results (Planck Collaboration et al. 2020).

2 MIGHTEE DATA

In this work, data from the MeerKAT telescope’s MIGHTEE survey (Jarvis et al. 2016) is used to make a statistical measurement of the H I signal at low z and on small scales (smaller than about 1 Mpc) via the H I power spectrum. The details of the specific MIGHTEE survey data are discussed below.

2.1 The MIGHTEE Survey

The MIGHTEE Survey¹ is one of the Large Survey Projects (LSPs) conducted using the MeerKAT telescope. It covers four well-studied extragalactic fields, namely COSMOS², XMM-LSS, CDFS, and ELAIS-S1, with a total observed area of about 20 deg². These various fields also have the potential to be used for multi-wavelength studies, which is a good trade-off for the fact that it is shallower in comparison to the complementary, deeper LADUMA Survey (Baker et al. 2018), which will go to much higher redshifts despite covering a much smaller patch of the sky. Importantly for the context of this study, the full MIGHTEE survey will reach similar depths ($\sim 1 \mu\text{Jy}$) as the planned SKA Observatory, thus making it a useful survey with which assess the level of sensitivity achievable for IM. To achieve its scientific goals, MIGHTEE conducts its survey by simultaneously making continuum (Hale et al. 2025), polarimetry (MIGHTEE-pol) (Taylor et al. 2024), and spectral-line (MIGHTEE-H I) (Heywood et al. 2024) measurements. Observations with the MIGHTEE survey have concluded, taking approximately 1000 hours of data in L-band over the four fields described above. In this work, the focus is on the use of various “Early-Science” data products, particularly the COSMOS central pointing (RA ~ 150.12 deg, Dec. ~ 2.2 deg) visibility data and MIGHTEE-H I galaxy detections obtained using said visibility data, over the low-redshift band ($0 < z < 0.09$, corresponding to the frequency range of 1310 MHz $< \nu < 1420$ MHz).

2.2 Visibility data

The data used comprises the interferometric visibilities observed with the MeerKAT telescope on the central pointing of the COSMOS field, as well as a catalogue of detected H I galaxies created using these interferometric observations (Ponomareva et al. 2023). The visibility data consist of three measurement sets (or data blocks) with a total on-source observation time of 17.45 hours. For the exact visibility data specifications, refer to Table 1. Although there are other blocks available over the COSMOS field, they correspond to different pointings and cannot be easily coherently averaged for the visibility-based power spectrum analysis. The initial two data blocks were observed with 4K (4096) channels over the L-band, with the last observed using the 32K (32768 channels) mode configuration of the telescope. The time resolution is 8 seconds. These data blocks are each divided into scans. The length of each of these scans in block 1524147354 and block 1525613583 is ~ 10 minutes, amounting to 37 and 31 scans for each, respectively. Block 1524147354, therefore, has a total observation time of 6.1 hours, while block 1525613583 has an observation time of 5.1 hours. The 32K block, block 1587911796, has longer scans of ~ 55 minutes, and a total observation time of 6.25 hours spread over 7 scans.

Being a core-heavy instrument, data observed with MeerKAT will be most sensitive to the larger range of cosmological (k) scales we are

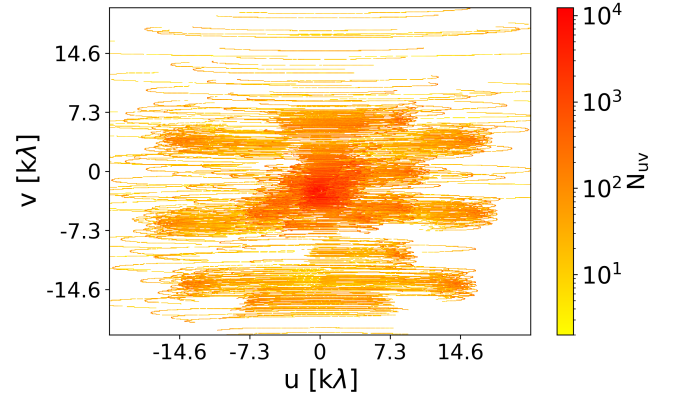


Figure 1. The uv distribution of the combined COSMOS field data used in this study at the central frequency of 1362.425 MHz. This distribution is shown in 2D, with the number of uv points displayed in the colour bar. The grid size used here is $\Delta u = \Delta v = 73\lambda$, where λ is the central wavelength of the band used in this study.

sensitive to. The core-concentration of MeerKAT is demonstrated by the uv distribution of the combined data blocks shown in Figure 1. For this study, we use the calibrated, flagged, and reduced measurement sets. The reduction process for this visibility data is described in Maddox et al. (2021) for the 4K data blocks, and in Heywood et al. (2021) for the 32K data block. We do not repeat such processes before putting the visibility data through the gridding, averaging, and power spectrum estimation pipeline discussed in Section 3. We make use of the frequency channels stored in the observed measurement sets over the range 1310 - 1420 MHz. From this selection of data blocks, we choose a relatively RFI-free region spanning approximately 1332.64 - 1392.20 MHz ($0.020 < z < 0.066$), resulting in a bandwidth of about 60 MHz. This range was chosen to match the redshift region where we have a complete catalogue of H I detected galaxies (Ponomareva et al. 2023). In 4K resolution, this results in 284 channels. To ensure data uniformity, the 32K data block, 1587911796, was reduced to 4K by averaging over every 8 frequency channels, thus allowing us to coherently combine and average the data from all three data blocks for the power spectrum estimation.

2.3 H I galaxy detections

In addition to the visibility data, a catalogue of detected H I galaxies from the MIGHTEE data is used in this study. The catalogue forms part of the outputs of the Early Science data processing for MIGHTEE-H I described in Ponomareva et al. (2023). It comprises H I detections on both the single COSMOS pointing and three overlapping pointings on XMM-LSS.

These detections were made, in the first instance, visually, with no guidance, on imaged cubes using the Cube Analysis and Rendering Tool for Astronomy (CARTA³) software suite. Once the positions and frequencies of each source are known, cubelets of each galaxy are extracted around the sources from the main cube. These cubelets are then processed by the source-finding and parametrisation tool SOFIA (Serra et al. 2015). Masks are created around the emission from the frequency channels that correspond to the galaxy sources.

¹ <https://www.mighteesurvey.org/>

² <https://cosmos.astro.caltech.edu/>

³ <https://cartavis.github.io/>

Block ID	Date (UT, J2000)	R.A.	Dec.	t_{obs} (on-source) (h)	N_{chan}	N_{ant}	Primary calibrator	Secondary calibrator
1524147354	2018-04-19	10 ^h 00 ^m 28 ^s .6s	+02°12'21''	6.1	4096	64	J0408-6545	3C237
1525613583	2018-05-06	10 ^h 00 ^m 28 ^s .6s	+02°12'21''	5.1	4096	62	J0408-6545	3C237
1587911796	2020-04-26	10 ^h 00 ^m 28 ^s .6s	+02°12'21''	6.25	32768	59	J0408-6545	3C237

Table 1. The MIGHTEE Early Science COSMOS central pointing visibility data sets used in this work. The table is adapted from [Heywood et al. \(2021\)](#).

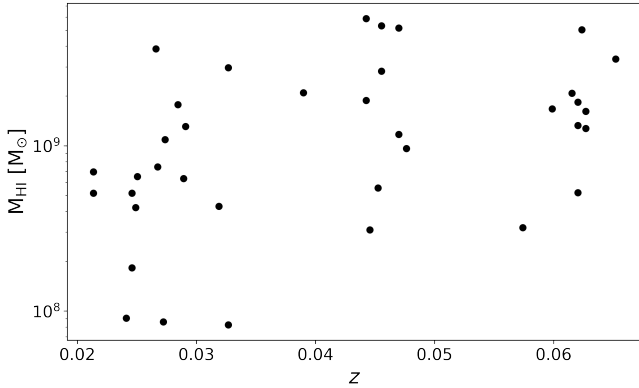


Figure 2. The H I masses, M_{HI} , for the selected galaxies from the full MIGHTEE-H I Early Science catalogue plotted at their respective redshifts, z . The sample shown contains galaxies on the central COSMOS pointing only and is sourced over a redshift range that aligns with the frequency range chosen for the visibility data.

After masking, the flux is summed, the central frequency of individual sources is calculated, and this H I flux, S , is then subsequently converted to H I mass, M_{HI} , using the relation from [Meyer et al. \(2017\)](#):

$$\left(\frac{M_{\text{HI}}}{M_{\odot}}\right) = \frac{2.356 \times 10^5}{1+z} \left(\frac{D_L}{\text{Mpc}}\right)^2 \left(\frac{S}{\text{Jy km/s}}\right), \quad (1)$$

where D_L is the luminosity distance to the source at redshift z , and S is the flux calculated from the individual cubelets for each source.

On the COSMOS pointing specifically, there are 80 detections over a redshift range of $0.02 < z < 0.09$, and spanning a H I mass range of $4 \times 10^7 M_{\odot} \lesssim M_{\text{HI}} \lesssim 10^{10} M_{\odot}$. The catalogue includes the measured velocity width corresponding to the point of the global H I profile at 50% peak flux density, also known as W_{50} , values. This W_{50} represents the maximum rotational velocity measured from a resolved rotation curve of a given galaxy, i.e., $V_{\text{max}} = W_{50}/2 \sin(i)$, where i is the inclination angle of said galaxy ([Ponomareva et al. 2021](#)). The details of the construction of the overall catalogue are described in [Maddox et al. \(2021\)](#), with additional details on how the W_{50} values were measured found in [Ponomareva et al. \(2021\)](#). Further, detailed H I studies making use of the data in this catalogue of detections can be found, for instance, in [Rajohnson et al. \(2022\)](#); [Tudorache et al. \(2022\)](#); [Pan et al. \(2022\)](#); [Ponomareva et al. \(2023\)](#).

Out of the 80 galaxies detected on the COSMOS field, 37 galaxies are in the 0.02 - 0.066 redshift range of interest. They are used to compare with the power spectrum estimation from the visibility data (see Section 4). One caveat worth mentioning here is that there may be galaxies that lie just beyond the frequency range that may leak a few channels into this range because of their width. Despite this, the effect of this will be negligible overall when comparing power

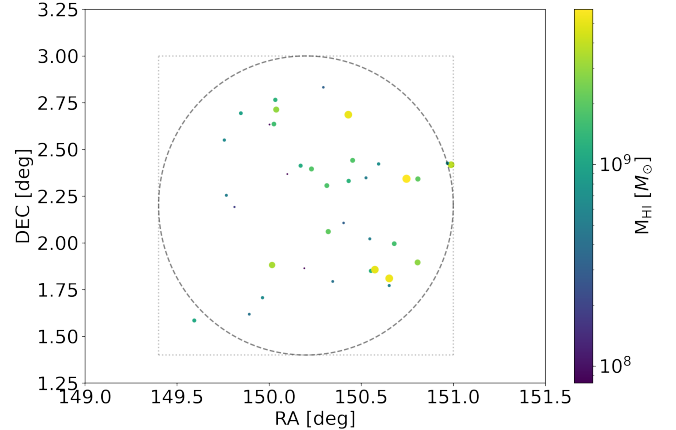


Figure 3. The H I masses, M_{HI} , and positions for each galaxy selected in the sub-band from the catalogue in R.A. and Dec. The dashed circle corresponds to the main lobe of the MeerKAT primary beam at 1362.425 MHz, while the dotted square denotes the edges along the Right Ascension and Declination maximum and minimum limits of the box in which the galaxy masses are placed (see Section 4).

spectra. The measured H I masses for each of these galaxies along redshift are shown in Figure 2, with an accompanying plot for R.A. and Dec. shown in Figure 3. Given the redshift range, as well as the area along R.A. and Dec., we estimate a cosmological volume of $\sim (389 \text{ Mpc}/h)^3$, or 1254 Mpc^3 . For 37 galaxies, this corresponds to a galaxy density per Mpc^3 , n_{gal} , of $\sim 0.03 \text{ Mpc}^{-3}$.

3 H I POWER SPECTRUM FROM THE MIGHTEE VISIBILITY DATA

This section discusses the methodology used to estimate the H I power spectrum on the MIGHTEE calibrated and processed visibility data. While the details discussed here are comprehensive, some useful complementary references to the technical details about the pipelines discussed below can be found in [Paul et al. \(2021\)](#); [Chen et al. \(2022\)](#); [Paul et al. \(2023\)](#).

3.1 Delay spectrum pipeline and power spectrum estimator

Here, we describe the methodology employed to produce the 3D power spectrum cube on the interferometric data observed using MeerKAT. This methodology was first developed in [Paul et al. \(2021\)](#), and has undergone improvements since then ([Paul et al. 2023](#)). From this 3D power spectrum, a methodology is described to calculate the subsequent cylindrical-averaged (2D) and spherically-averaged (1D) power spectra. The paper discussed the possibility of estimating the H I power spectrum by producing simulations of MIGHTEE observations of the COSMOS field informed by the observational

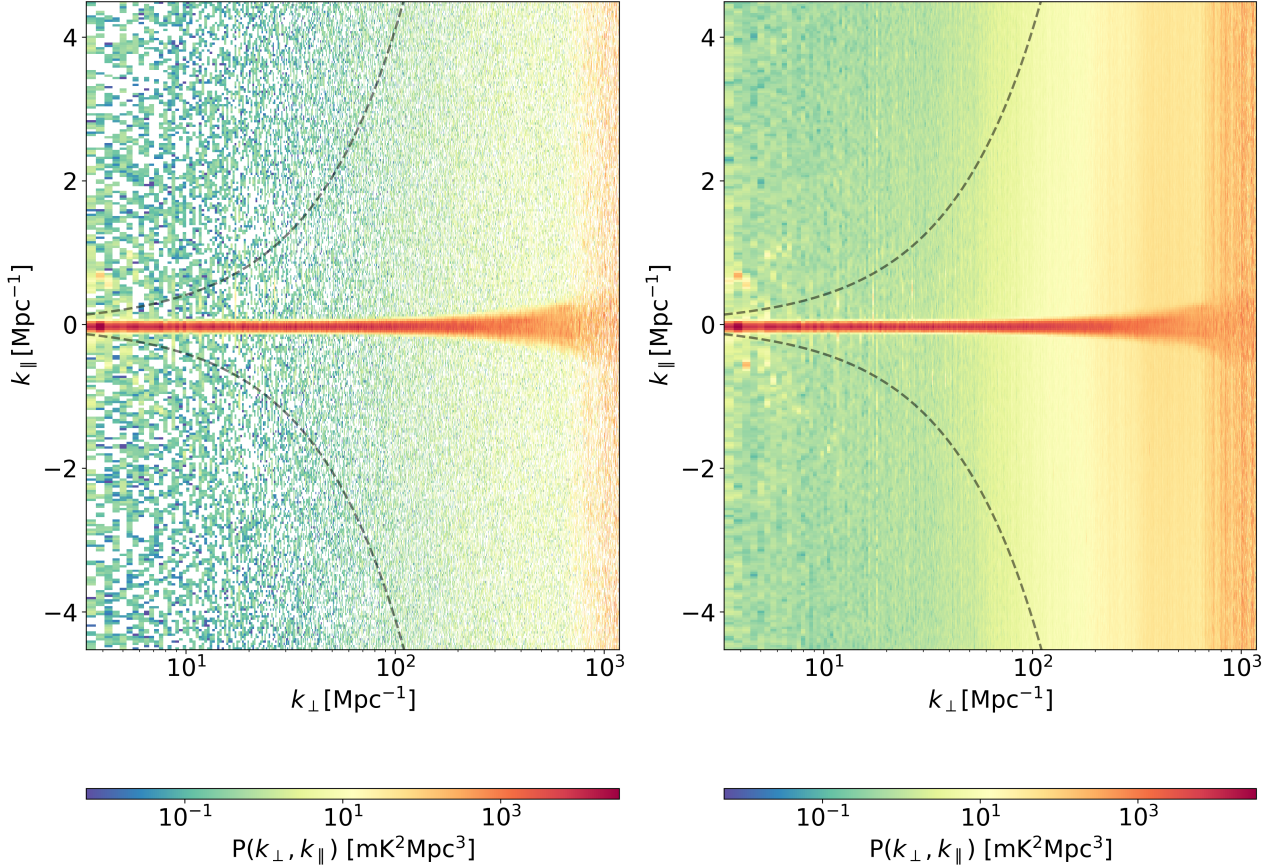


Figure 4. The Stokes I cylindrical cross-correlation (left) and auto-correlation (right) power spectra of the combined 17.45h of MIGHTEE COSMOS Early Science visibility data before any contamination removal is applied to the 3D power spectrum cube, $P(\mathbf{k}_\perp, k_\parallel)$. Also shown is the horizon limit, $k_\parallel^{\text{horizon}}(k_\perp)$ as a dashed grey line for $\pm k_\parallel$.

parameters and first measurement sets from the survey itself. Since then, the proposed methodology has also been used in the analysis of ~ 96 hours of MeerKAT data observed on a single pointing on the DEEP2 field (Mauch et al. 2020) in Paul et al. (2023) to make a tentative detection of the $H\text{I}$ signal in auto-correlation.

In this work, applying the techniques and lessons learnt so far to a set of interferometric observations which can be directly compared to $H\text{I}$ detections made on the data, we can further validate the methods employed to obtain the Paul et al. (2023) results, in addition to being a means of providing an estimate of the $H\text{I}$ power spectrum on the MIGHTEE data at low redshift ($z < 0.1$).

The first step in the pipeline is to average all the visibilities into a grid in the (u, v) plane at each frequency channel, ν . This is done for both the Stokes I visibility data and Stokes V, as described later. We choose 1500 grid points and select $\Delta u = \Delta v = 73\lambda$, which approximately corresponds to the width of the MeerKAT primary beam in k_\perp space at the central frequency (~ 1362 MHz) of the band. We consider two scenarios:

(i) A single grid on which all the visibility data is gridded and averaged. Power spectra estimations on this are designated as auto-correlation power spectra, or "Visibilities (total)", to denote power spectra derived from this single-grid, combined MIGHTEE visibility data in some comparative power-spectrum results.

(ii) In the cross-correlation case, instead of combining all the visibility data on one grid, each consecutive 8-second time stamp

of data is placed on one of two visibility grids. We denote these visibility grids as "odd" and "even". The power spectra estimated on the cross-correlation of these grids are labelled as "Visibilities Cross" or "Visibilities (odd \times even)".

Since the noise in each grid is not expected to correlate, this cross-correlation eliminates the noise bias. Hence, where there is predominantly noise in the data, we expect the power spectrum to be consistent with zero. At the same time, where we have sufficient sensitivity, our estimator should yield the unbiased $H\text{I}$ signal power spectrum amplitude. In the auto-correlation case, to remove the thermal noise contribution, it has to be modelled through simulations based on the observational parameters from the data (this is discussed further in Section 3.3).

The gridded visibilities are then Fourier transformed along the frequency axis and multiplied by their conjugate (or by the conjugate of the second grid in the case of cross-correlation) to obtain the 3D power spectrum in units of $\text{Jy}^2 \text{Hz}^2$. This $uv\tau$ cube is then multiplied by normalisation factors to obtain the power spectrum in cosmological units of $\text{Mpc}^3 \text{mK}^2$. Mathematically, the delay power spectrum can be written as (Morales & Hewitt 2004; McQuinn et al. 2006; Parsons et al. 2012b; Pober et al. 2013; Thyagarajan et al. 2013; Parsons et al. 2014; Thyagarajan et al. 2015; Paul et al. 2016)

$$\hat{P}_D(\mathbf{k}_\perp, k_\parallel) = \left(\frac{\lambda^2}{2k_B} \right)^2 \frac{A_e}{\lambda^2 B} \frac{r_y^2 \Delta r_y}{B} \Re \{ \tilde{V}_i(\mathbf{u}, \tau) \tilde{V}_j^*(\mathbf{u}, \tau) \}, \quad (2)$$

where \mathbf{k}_\perp is composed of the k_x and k_y angular scales and is given by $\mathbf{k}_\perp = 2\pi\mathbf{u}/r_\nu$, with $\mathbf{u} = (u, v)$ and r_ν the comoving distance at the central redshift of the observation, z . The central wavelength of the observed bandwidth is λ , k_B is the Boltzmann constant, A_e is the effective area of the dish, B is the bandwidth of the observation and Δr_ν is the comoving width corresponding to this bandwidth. For this power spectrum, we take the real part of the visibility correlation, $\Re\{\tilde{V}_i\tilde{V}_j^*\}$, where i and j correspond to the two visibility grids generated for the cross-correlation case, and $i = j$ for the auto-correlation. The above result is valid in the regime where there is negligible redshift evolution along the light cone and also necessarily relies on the flat sky approximation (Chen et al. 2021). To estimate the 1D power spectrum from the 3D power spectrum cube given by $\hat{P}_D(\mathbf{k}_\perp, k_\parallel)$, an inverse noise variance weighted spherical average is taken in logarithmic k bins, Δk_i , which can be expressed as (Paul et al. 2023)

$$\hat{P}_D^i(k) = \sum_j P_D^j w_j / \sum_j w_j, \quad (3)$$

where $w_j = 1/\sigma_{j, P_{TN}}^2$ are the thermal noise variance weights (discussed further in Section 3.3) and P_D^j are the 3D power spectrum amplitude values, j , in the selected k bin. Further, the error on this power spectrum estimate can be derived from the sampling variance (Paul et al. 2023),

$$(\Delta \hat{P}_D^i)^2 = \sum_j (P_D^j - \hat{P}_D^i)^2 w_j^2 / \left(\sum_j w_j \right)^2. \quad (4)$$

The cylindrically-averaged (2D) power spectrum can also be estimated similarly by applying the same inverse noise variance weighting and binning cylindrically in transverse and line-of-sight k modes, (k_\perp, k_\parallel) , giving an estimator of the form

$$\hat{P}_D^i(k_\perp, k_\parallel) = \sum_j P_D^j(k_\perp, k_\parallel) w_j(k_\perp, k_\parallel) / \sum_j w_j(k_\perp, k_\parallel), \quad (5)$$

which collapses the 2D k_\perp plane while performing the above averaging and noise weighting. To make use of foreground avoidance, modes are sampled above the horizon limit (Datta et al. 2010; Parsons et al. 2012b; Liu et al. 2014; Thyagarajan et al. 2013, 2015),

$$k_\parallel = \frac{r_\nu(z)E(z)H_0}{c(1+z)} \sin(\theta) k_\perp, \quad (6)$$

where H_0 is the Hubble parameter at $z = 0$, $E(z) = H(z)/H_0$ and c is the speed of light in a vacuum. In this work, we use $\sin(\theta) = 1$ as this corresponds to the maximum delay, e.g. largest k_\parallel for the foreground wedge. Any spectrally smooth signal should be well below this boundary. This ensures that, for the power spectrum estimation, modes are sampled well above the region where we expect foregrounds to be located in the 3D power spectrum cube, giving minimal spillover into the H I window. At $z \sim 0.042$, this limit reduces to $k_\parallel \simeq 0.041 k_\perp$. This is shown plotted on the cylindrical power spectra as a dashed curve throughout the paper for both $\pm k_\parallel$.

Figure 4 shows the Stokes I cylindrical power spectra estimated for both auto- and cross-correlation of delay-transformed visibility grids. Also shown is the horizon limit as a dashed line along k_\perp for both $\pm k_\parallel$. The main foreground wedge is mainly confined below the horizon limit due to the relatively small size of the MeerKAT beam. The Early Science COSMOS data have been put through a comprehensive calibration and flagging process, and as a result, we have a clean H I window over which to estimate power spectra.

Despite this, some residual contamination appears to be present above the theoretical horizon limit when examining the cylindrical power spectra. This is seen in the combined data as well as in each data block. It is present in both auto- and cross-power spectra, although it is more obvious in the auto-power spectra, as can be seen from the figure. The strongest contamination is localised below $k_\parallel \sim 1 \text{ Mpc}^{-1}$ and $k_\perp \sim 6 \text{ Mpc}^{-1}$. This corresponds to the region in which the first two cylindrical k bins of the estimator are selected, so we expect these bins to have some contamination if no extra flagging is applied. We will next discuss our approach to dealing with this contamination in the 3D power spectrum cube before making estimates of the 1D H I power spectrum.

3.2 Removal of low-level contamination

The contamination found in the cosmology window of our 2D power spectrum only affects a few pixels but has the potential to contribute to the bulk of the power in the k bins over which we estimate the 1D power spectrum. At the same time, it is broadband and of a low enough level to evade standard flagging approaches. Therefore, we adopt the approach of flagging the contamination at the 3D power spectrum level. We have a total of $\sim 3 \times 10^7$ 3D \mathbf{k} modes above the horizon limit we choose in our data, and we expect these to be predominantly noise-dominated. By comparing these 3D values to the expected noise distribution, we can identify and flag extreme outliers. If this number is small, the impact on signal loss should be negligible. Therefore, we create a flag mask, based on detailed thermal noise simulations, to be applied to the voxels in the 3D auto-power spectrum cube. This is done before performing any power spectrum averaging on the 3D cube to obtain 2D and 1D power spectrum estimates. The flag criterion is given by

$$|P_D(\mathbf{k}_\perp, k_\parallel) - \bar{P}_{TN}(\mathbf{k}_\perp, k_\parallel)| > N \times \sigma_{P_{TN}}(\mathbf{k}_\perp, k_\parallel), \quad (7)$$

That is, we flag voxels when the difference between the delay power spectrum, P_D , and the average expected thermal noise power spectrum, \bar{P}_{TN} , at $(\mathbf{k}_\perp, k_\parallel)$ is greater than some integer multiple, N , of the standard deviation, $\sigma_{P_{TN}}$, of this set of thermal noise power spectra generated from the thermal noise visibility realisations (we discuss these realisations further in Section 3.3). This procedure is done on the 3D auto-power spectrum cube, P_D , of both the "odd" and "even" visibility grids, and then the masks generated on each are combined. If voxels are flagged in the "odd" or "even" case, then the final mask will have that voxel flagged (regardless of whether or not it is only flagged in one or the other of the odd/even cases). Further, we used $N = 5$, which should only pick up extreme outliers while eliminating most of the trace contamination that shows up in the Stokes I power spectrum.

Guaranteeing that our data are indeed free of outliers might be subject to some discussion. In this case, visual inspection on the 2D power spectrum helped us identify some "hot" pixels that should not be present if the data were H I or noise-dominated. We have a good understanding of how both the H I and noise should be distributed at the 3D power level for our dataset. Any strong outliers from the expected distribution (e.g., by looking at the histograms) are almost certainly due to contamination. Of course, this will become more difficult if the contamination level is close to the noise level. Another way to spot contamination is to look at clear patterns in the flag fraction, as can be seen later in Section 5.4. Ideally, this contamination should be picked earlier in the data processing, but wide-band, low-level RFI might very well only show up at the 3D power spectrum level, after some visibility averaging is done. Further cases for N

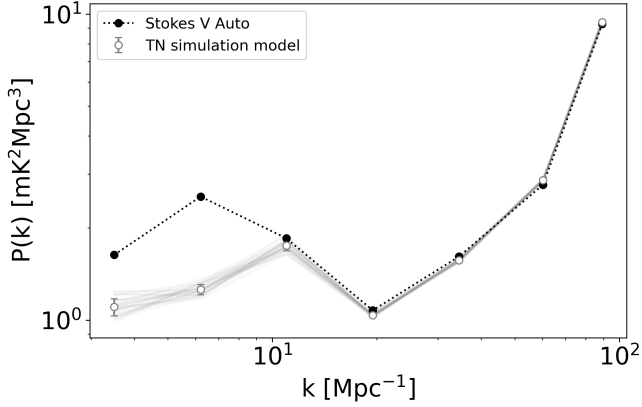


Figure 5. Comparison between the Stokes V and refitted simulated thermal noise 1D auto-power spectra. The increased amplitude we observe at $k \lesssim 10 \text{ Mpc}^{-1}$ for Stokes V is primarily due to leakage from Stokes I, resulting in the discrepancy in the two power spectra. Beyond this, the power spectra are consistent across all k scales.

and the power spectrum results of this are discussed in Section 5.4. Again, it is important to note that the $H\text{I}$ signal is highly anisotropic at these scales, so the impact of this flagging will depend on where it is applied, at least in terms of the 2D power spectrum. A comparison with any model should be done by applying the same flags to the model in the 2D space before any spherical averaging.

With a means to grid, average, and transform the visibility data and then subsequently estimate power spectra with thermal noise weighting and contamination flagging, these methods can be applied to the Stokes I data. We next discuss the thermal noise simulations.

3.3 Thermal noise simulations

Thermal noise simulations are required to effectively apply the estimator to the Stokes I (or V) data, as it relies on these simulations for the noise weighting, as well as removing contamination found in the $H\text{I}$ window of the power spectrum cube generated on the visibility data. This is done at the visibility level. For each baseline, time stamp, and frequency channel, the thermal noise is assigned randomly from a complex Gaussian distribution with a mean of zero, $\mu_{\text{TN}} = 0$, and a standard deviation given by the radiometer equation (Campbell 2002; Morales 2005):

$$\sigma_{\text{TN}} = \frac{2k_{\text{B}}T_{\text{sys}}}{A_e \sqrt{\delta\nu \delta t}}, \quad (8)$$

where T_{sys} is the system temperature of the instrument, A_e is the effective area of the dishes and $\delta\nu$ and δt are the frequency and time resolutions, respectively. The quantity A_e/T_{sys} is known as the natural sensitivity. It is particularly crucial for ensuring that the simulated thermal noise amplitude is accurate when comparing it to the Stokes I power spectrum amplitude.

The reported⁴ MeerKAT natural sensitivity for the selected frequency range is $6.22 \text{ m}^2/\text{K}$. Since the reported value from MeerKAT and that obtained from the data itself may be different due to differing system temperature, it needs to be corrected. To do this, we compare

⁴ <https://skaafrica.atlassian.net/wiki/spaces/ESDKB/pages/277315585/MeerKAT+specifications>

Visibility power spectrum: odd \times even

k bin [Mpc^{-1}]	Total	Sampled	Percentage Sampled
2.46 – 4.34	1034	982	94.97%
4.34 – 7.77	5062	4944	97.67%
7.77 – 13.8	17900	17606	98.36%
13.8 – 24.6	48548	47928	98.72%
24.6 – 43.7	132944	131365	98.81%

Table 2. Table summarizing the k bins, total k modes in each bin, and the percentage of these that are sampled after applying the 5σ cut for the visibility data cross-power spectrum (odd \times even).

simulated thermal noise power spectra amplitudes based on the observation parameters of our data to the power spectrum obtained from the Stokes V data. At least at large k values, we expect such data to be noise-dominated. The Stokes V data are put through the same gridding and averaging procedures as described for Stokes I. The 1D power spectrum is then compared to the 1D thermal noise power spectrum averaged over 10,000 realisations put through the same procedures described for Stokes I and Stokes V. The ratio of the 1D thermal noise power and Stokes V power at $k > 10 \text{ Mpc}^{-1}$ is then used as a factor to rescale the initial value of A_e/T_{sys} . Doing so results in a value of $6.75 \text{ m}^2/\text{K}$, which is still consistent with what we expect for MeerKAT.

Once a refitted value for the natural sensitivity is obtained, the 10,000 realisations of the thermal noise simulations are used as a model of the thermal noise present in the data. The spherically averaged noise power spectrum is shown in Figure 5 and compared to the 1D power spectrum from the Stokes V data. The noise increases for large k_{\perp} due to the smaller number of long baselines. At $k \gtrsim 10 \text{ Mpc}^{-1}$, there is good agreement between the power spectra as expected, since the Stokes V signal will be noise-dominated. Below that, we see more power from Stokes V which should be primarily leakage from Stokes I. We then use the variance over the set of thermal noise power spectrum realisations, $\sigma_{P_{\text{TN}}}^2$, as the weights, w_j , in the power spectrum estimator.

3.4 Power Spectrum Results

We now turn to the power spectrum results using the pipeline described above. Figure 6 shows the cylindrical power spectra for auto-correlation and cross-correlation of the visibilities. Both cases are shown after 5σ flags calculated on the data using Equation 7 have been applied to the 3D power spectrum cube. The flagging percentage in the region of uv space corresponding to the region above the horizon line in $P(k_{\perp}, k_{\parallel})$ is shown in Figure 7, demonstrating that the contamination that is flagged out by the criterion given in Equation 7 flags k modes in the cube that are localised at $k_{\perp} \lesssim 20 \text{ Mpc}^{-1}$, which corresponds to a radius in uv -space of $\sim 2700 \lambda$. The percentage of k modes flagged by this criterion in each k bin is shown in Table 2. For the visibility data, the flagging removes $\sim 5\%$ within the first k bin and $\sim 2\%$ in all subsequent bins. This indicates that the flagging is not extensive and should not result in significant signal loss.

In addition to considering the power spectrum estimated on the cross-correlation of delay-transformed visibility cubes (even \times odd), we also consider the auto-power of the combined visibility data placed in a single $uv\tau$ cube (odd + even). To include this case in the comparison, the auto-power spectrum cube is also flagged using the 5σ criteria to remove the contamination. After this, a thermal noise power spectrum model is subtracted from the 1D auto-power spectrum after applying the power spectrum estimator given in Equation

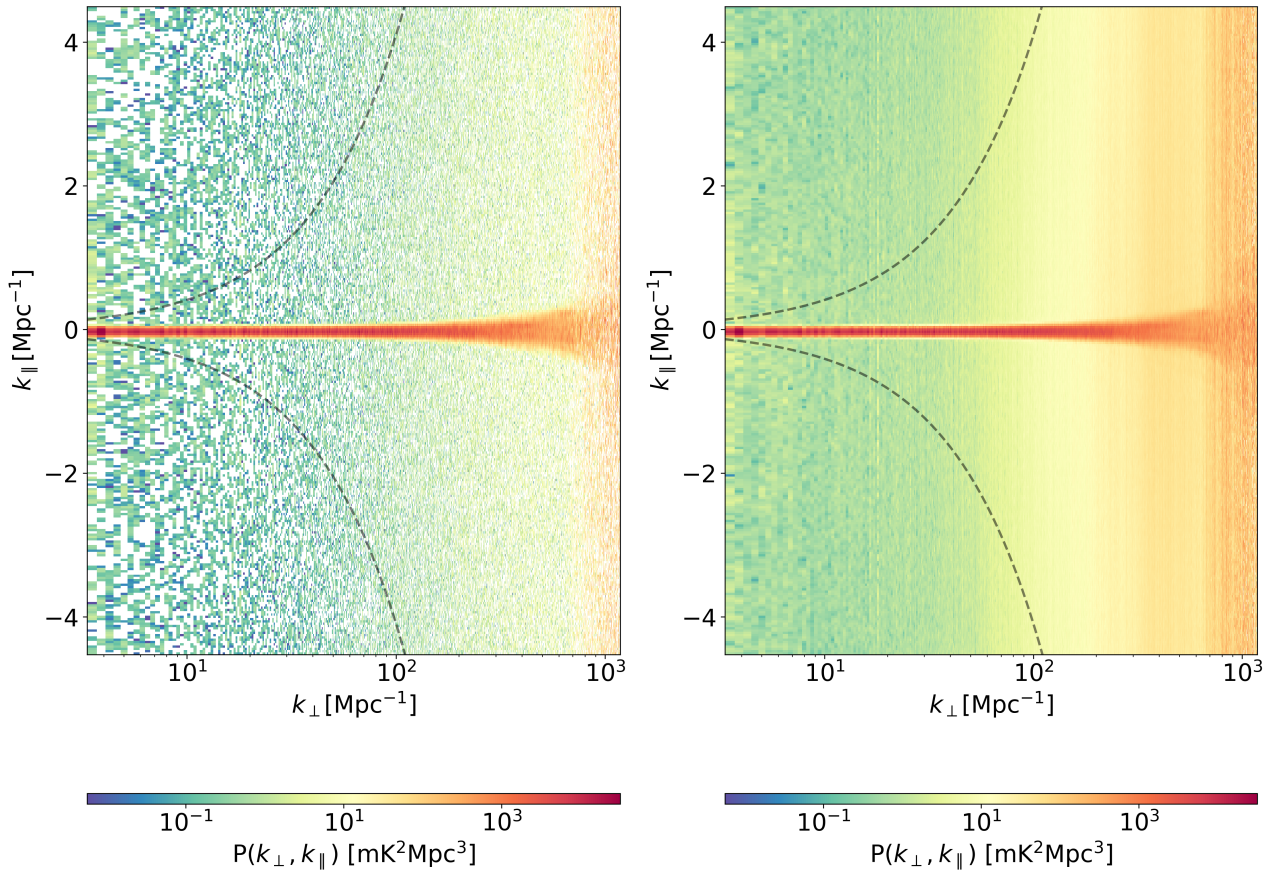


Figure 6. The Stokes I cylindrical power spectrum for the combined measurement set data after the 5σ cut has been applied for both cross- (left) and auto-correlation (right) cases. Also shown is the horizon limit, $k_{\parallel}^{\text{horizon}}(k_{\perp})$ as a dashed grey line for $\pm k_{\parallel}$. The contamination present in the same region above the horizon limit in the power spectrum shown in Figure 4 was removed after applying this cut in either case (cross or auto).

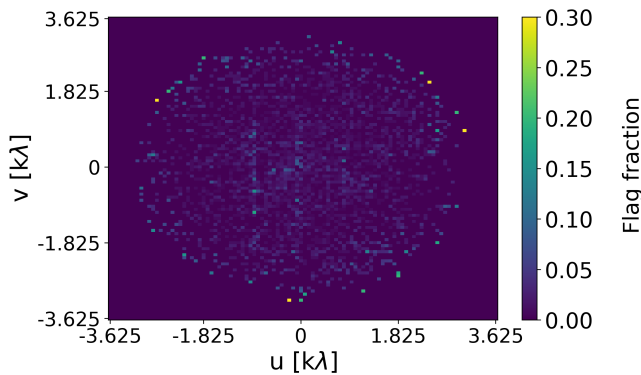


Figure 7. The uv -plane flagging fraction in the central portion of the uv grid for the measurement set data used. The maximum fraction has been set to 30% on the colour bar to clearly show lower level flagging applied by the 5σ cut, especially in the central region of the uv distribution corresponding with small k_{\perp} .

3. The model that is subtracted from the auto-power spectrum is the mean of the 10,000 thermal noise realisations described in Section 3.3. Assuming that the estimated value of A_e/T_{sys} accurately represents the noise in our data, this average will be a good approximation and can, therefore, be subtracted from the Stokes I auto-correlation power spectrum.

Figure 8 shows a comparison of the 1D cross-power spectrum and auto-power spectrum estimated from the visibility data after applying a 5σ cut. Included in the comparison is the power spectrum of the cross-correlated visibility data before the contamination flagging is performed. The shaded open circles show the negative power amplitudes. The auto-correlated visibility power spectrum should be an upper limit on the expected H I power spectrum on these scales. It is interesting that, other than in the second and fourth k bins, the thermal noise-subtracted auto-power is consistently higher than the power spectrum on the cross-correlation of visibilities before the 5σ flagging is applied. This is likely due to small inaccuracies in the thermal noise power spectrum modelling at small k , despite its close correspondence with the Stokes V power spectrum at $k \gtrsim 20 \text{ Mpc}^{-1}$. Additionally, it could also indicate that there is residual contamination present in the auto-correlation power spectrum, which is ultimately reduced when taking the cross-correlation. The cross power spectrum estimate after 5σ flagging shows a significant drop in the second and third k bins. The smaller drop in the first bin might indicate that there is still some contamination left after the 5σ cut. The estimated power spectrum values after the 5σ flagging are shown in Table 3 with an overall signal to noise of ~ 13 . As we will see later, this measured power spectrum is consistent with the power from the detected H I galaxies. Moreover, there is a clear non-zero signal when cross-correlating with the H I galaxy data, as expected if the majority of the signal in the cleaned visibility dataset is from H I. However, the power spectrum result presented here might still be biased, both

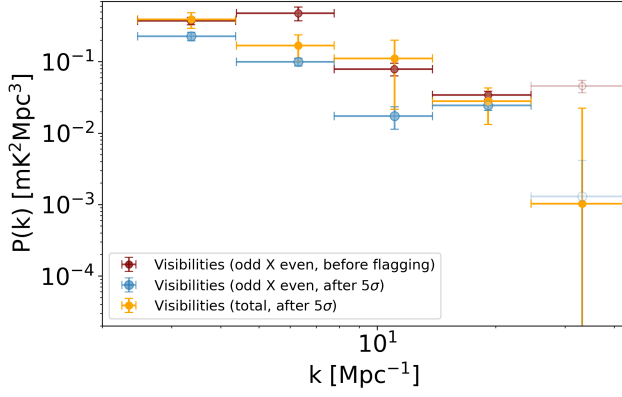


Figure 8. Comparison of the 1D power spectrum estimate from the visibility data before and after applying the 5σ flagging to the 3D power spectrum. Included is the auto-correlation power spectrum after doing a noise model subtraction and applying the same 5σ flags.

due to residual contamination and possible signal loss. This is further discussed in the validation sections.

4 VALIDATIONS: H I POWER SPECTRUM FROM A BOX OF DETECTED H I GALAXIES

In this section, we develop a pipeline to measure the H I galaxy power spectrum, which will be used to compare to our visibility-based approach. The procedures in this section describe a method of going directly from the information provided in the galaxy catalogue described in Section 2.3 such as H I mass, M_{HI} , RA, Dec., redshift (z) and W_{50} to an H I intensity cube and then the H I power spectrum.

4.1 Temperature mesh assignment

The procedures applied to the catalogue to produce the temperature cube/mesh and the power spectrum estimation steps can be summarized as follows:

- Galaxies within the redshift range ($0.02 < z < 0.066$) are selected along with their R.A., Dec., and M_{HI} .
- The galaxies are transformed from sky coordinates (R.A., Dec., z) to Cartesian coordinates (L_x, L_y, L_z) in Mpc/h units.
- The Cartesian coordinates and the galaxy masses themselves are added to a mesh grid using the Nearest Grid Point (NGP) mass-assignment scheme. This scheme can be expressed as (Jing 2005; Cui et al. 2008; Colombi et al. 2009; Cunningham & Wolz 2024):

$$W_{\text{NGP}}(\mathbf{x}) = \begin{cases} 1, & \text{for } |\mathbf{x}| < \frac{1}{2} \\ 0, & \text{otherwise,} \end{cases} \quad (9)$$

where \mathbf{x} is the distance of the particle (in this case, a given galaxy from the catalogue) from the centre of the grid point, normalised by the cell (pixel) size. The pixel size selected for this is 0.05 Mpc/h to ensure that a pixel can realistically contain all the H I for each galaxy. This choice is made based on the expected H I sizes of the MIGHTEE-detected galaxies according to the H I size-mass relation (Rajohnson et al. 2022). In our case, even the highest-mass galaxies have a D_{HI} that is smaller than the 0.05 Mpc/h pixel size, and so

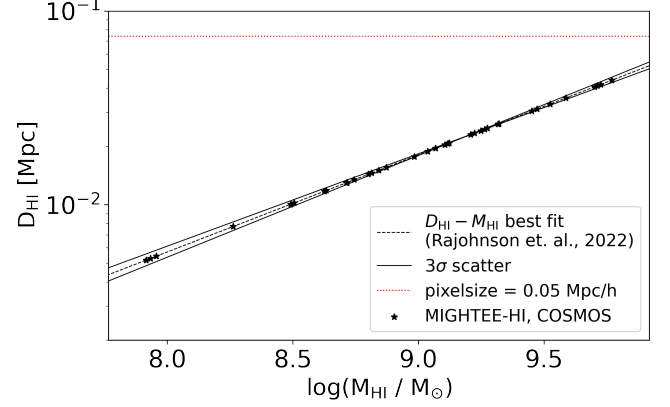


Figure 9. The best-fit H I size-mass relation ($D_{\text{HI}} - M_{\text{HI}}$) from Rajohnson et al. (2022) with 3σ scatter, plotted with the predicted H I sizes of the selected galaxies on the central COSMOS pointing according to their H I masses. The red dotted line shows the pixel size selected for the mesh in Mpc.

requires no further interpolation of H I mass into neighbouring cells in the mesh grid, hence our use of the NGP mass-assignment scheme. This is illustrated in Figure 9 via the expected H I size calculated from the H I masses of each galaxy in the catalogue based on the fit provided in Rajohnson et al. (2022).

- For completeness, higher-order mass assignment schemes are also tested without applying any aliasing corrections to see the deviation from the NGP assignment scheme case. In particular, the Cloud-in-Cell (CIC) and Triangular-Shaped Cloud (TSC) mass assignment schemes are tested. These are given in real space as

$$W_{\text{CIC}}(\mathbf{x}) = \begin{cases} 1 - |\mathbf{x}|, & \text{for } |\mathbf{x}| < 1 \\ 0, & \text{otherwise} \end{cases} \quad (10)$$

$$W_{\text{TSC}}(\mathbf{x}) = \begin{cases} \frac{3}{4} - |\mathbf{x}|^2, & \text{for } |\mathbf{x}| < \frac{1}{2} \\ \frac{1}{2} \left(\frac{3}{2} - |\mathbf{x}| \right)^2, & \text{for } \frac{1}{2} \leq |\mathbf{x}| < \frac{3}{2} \\ 0, & \text{otherwise} \end{cases} \quad (11)$$

The power spectrum results on the galaxy mesh grids comparing the various mass assignment schemes are shown in Figure 10. This comparison is done without including the spreading of M_{HI} along L_z . This is to ensure that the comparison is done without including any window functions along z which could induce suppression of the power spectra in addition to that imposed by the different mass assignment schemes. Also shown here is the H I shot noise power spectrum model given by (Chen et al. 2022)

$$P_{\text{SN}} = \bar{T}_{\text{HI}}^2 V \sum_i (M_{\text{HI}}^i)^2 / \left(\sum_i M_{\text{HI}}^i \right)^2, \quad (12)$$

where \bar{T}_{HI} is the average H I temperature, V is the volume of the mesh, and the sum is over the H I mass in the mesh. Since this model assumes point sources and does not include the effect of W_{50} along the line-of-sight or the smoothing along L_x and L_y induced by mass assignment, we expect it to be consistent with the power spectrum on the H I galaxies using the NGP scheme. We indeed see that the NGP power spectrum and shot noise model are consistent in Figure 10 for $k \gtrsim 10 \text{ Mpc}^{-1}$. A derivation of this

Visibility power spectrum: odd \times even (after 5σ cut)

k [Mpc^{-1}]	$P(k)$ [$\text{mK}^2 \text{Mpc}^3$]	$\sigma_P(k)$ [$\text{mK}^2 \text{Mpc}^3$]	$P(k)/\sigma_P(k)$
3.366	0.227	0.031	7.323
6.297	0.100	0.012	8.333
11.055	0.017	0.006	2.833
19.131	0.025	0.004	6.250
33.162	-0.001	0.003	-0.333

Table 3. Estimated 1D power spectrum values. Shown are the effective k at which the power spectrum amplitudes, $P(k)$, are quoted, as well as the errors, $\sigma_P(k)$, and the ratio of the amplitude to error, P/σ_P .

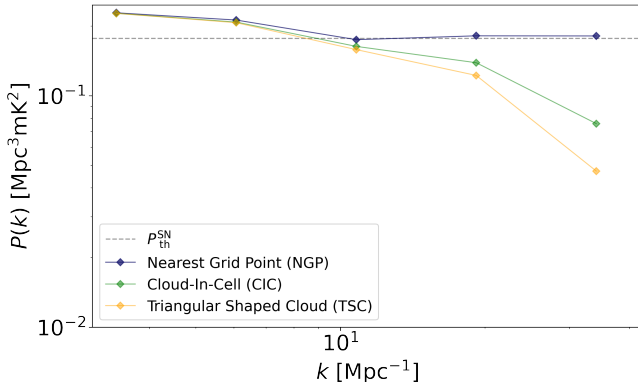


Figure 10. Comparison of the power spectrum using the standard mass-assignment schemes in `nbodykit`, using the standard power spectrum estimator on the H I galaxy mesh. This does not include the spreading of mass along L_z , any k mode-exclusion induced by the foreground avoidance, and the 5σ flagging or thermal noise weighting.

shot noise model can be found in Appendix A. When including all the effects, such as the line width, and given the large cell size, we found that the NGP scheme is the optimal option for our purposes.

- Once the galaxy H I masses have been placed in voxels, the mass is distributed along L_z using the characteristic width given by the W_{50} of each galaxy in the catalogue. Here, a choice for the shape is made as only a numerical value for the W_{50} is provided in the catalogue. Li et al. (2024) has shown that the choice of the shape of the profile has minimal effects on the power spectrum estimated from the galaxies, hence we make the choice of using a Boxcar function which evenly distributes the H I mass of each galaxy along L_z over the pixels which correspond to the characteristic length scale given by the W_{50} . The relation between this length scale and the W_{50} can be expressed as:

$$r_{\text{galaxy}} = \frac{W_{50}}{H(z)}(1+z), \quad (13)$$

where H is the Hubble factor at the redshift of the galaxy, z , in units of km/s/Mpc .

- The mesh now has the H I mass of each galaxy selected from the catalogue in units of M_{\odot} . This is converted to H I temperature using (Chen et al. 2022)

$$T_{\text{H I}}^{\text{pix}} = \frac{C_{\text{H I}}(z) M_{\text{H I}}^{\text{pix}}}{V_{\text{pix}}}, \quad (14)$$

where the conversion is done across the entire mesh at the central

frequency of the mesh, z_c .

- So far, the steps described above make use of tools in the `nbodykit`⁵ package (Hand et al. 2018), which is conveniently suited to dealing with the computations required for converting survey data into cosmological volumes ready for power spectrum estimation and other cosmological calculations.

- The H I temperature mesh cube is then used to obtain an estimate of the power spectrum using equations 3 and 4, with the same foreground avoidance applied using Equation 6, and taking comparative cases in which the same thermal noise weights, w_j , are applied. For the standard estimator on the H I temperature mesh, these weights are excluded, i.e., $w_j = 1, \forall j$. The thermal noise weighting and foreground avoidance help ensure that the estimated galaxy H I power spectrum is equivalent to the estimate obtained from the visibility data.

- Finally, to be able to apply the same windows and weights to this 3D power spectrum, we interpolate and extrapolate the $(k_{\perp}, k_{\parallel})$ galaxy cube to match exactly the one derived from the visibility data. The main issue is the perpendicular resolution of the galaxy box. In order to fix this, a simple extrapolation was made where higher k_{\perp} values were matched to the galaxy box maximum k_{\perp} . This is enough because 1) the foreground cuts remove most of the high k_{\perp} values, 2) we only show comparisons down to the galaxy box resolution, and 3) the shot noise will dominate at higher k_{\perp} .

4.2 Impact of flags and weights

We now discuss the impact of foreground avoidance, noise weights, and power spectrum flags on the H I galaxy power spectra. Since the H I power spectrum is highly anisotropic, especially on the scales considered in this work, any change in the selected $(\mathbf{k}_{\perp}, k_{\parallel})$ modes can impact the final 1D power spectrum. Figure 11 shows the effect of foreground avoidance on the mass spread (W_{50}) case. Note that for the case of no spread along L_z in which each galaxy's mass is confined to a single voxel, we do not expect foreground avoidance to have a significant effect on the overall amplitude. On the other hand, for the W_{50} case, the loss of low k_{\parallel} modes leads to a loss of power which becomes more significant at large k .

Figure 12 shows the effect of applying the 5σ flags. In this case, we flag the exact same 3D modes as the ones flagged on the visibility data. The difference between the flagged and unflagged cases is less than 5%. This is somewhat at odds with what we have seen with the full visibility data, where the power spectrum shows a larger drop as we increase the σ flagging. The comparison is non-trivial

⁵ <https://nbodykit.readthedocs.io/en/latest/>

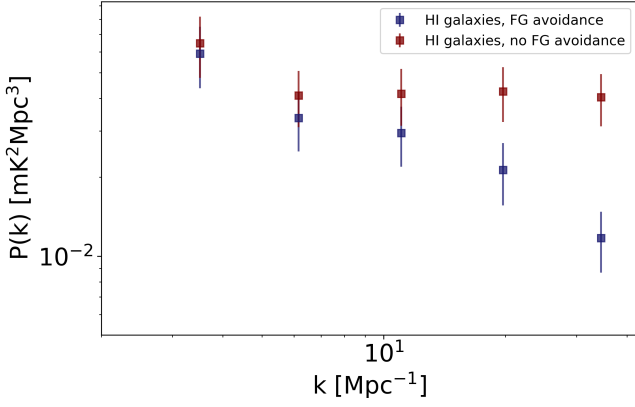


Figure 11. Comparing the $H\text{I}$ power spectrum from galaxies with and without foreground avoidance. This is done before applying the 5σ flags or the thermal noise weights.

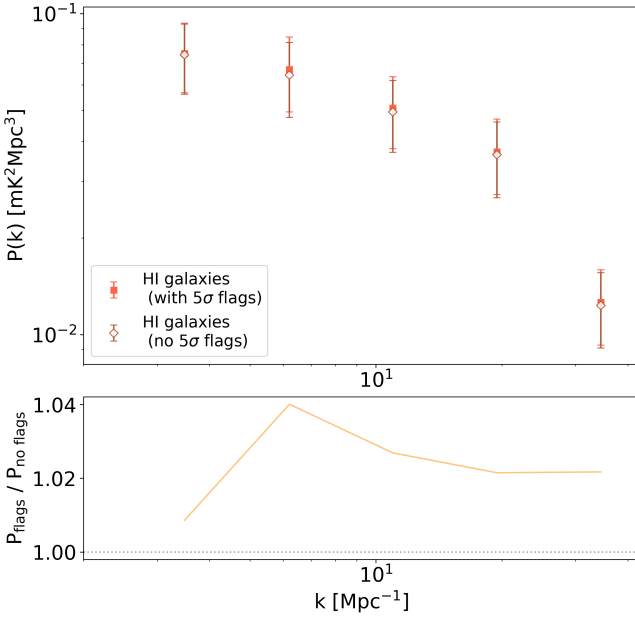


Figure 12. The $H\text{I}$ power spectrum estimated on the $H\text{I}$ galaxies comparing the cases of including and excluding the 5σ flags (top), as well as the ratio of the two cases (bottom) over the full k range.

because the 2D power spectrum is highly anisotropic. This is why we can even have the signal amplitude increasing slightly, as seen in this figure. Our understanding is that the "real" signal has power more "spread out" and closer to the horizon cut in comparison to our $H\text{I}$ galaxy only signal. That is also where most of the σ flagging is happening (Figure 23). On the other hand, the thermal noise weights have a much more significant impact on the estimated power spectrum. Specifically, these weights raise the power spectrum amplitude at $k \lesssim 20 \text{ Mpc}^{-1}$ as shown in Figure 13. This is because we have small k_{\perp} values contributing to these modes, which have low noise due to the large number of short baselines and therefore get "up-weighted". Above $k \sim 20 \text{ Mpc}^{-1}$, the noise will start dominating everywhere (Figure 5). The impact of these weights on the final averaged power spectrum arises from the strong anisotropies in the 3D power spectrum. Therefore, the same weights, flags, and

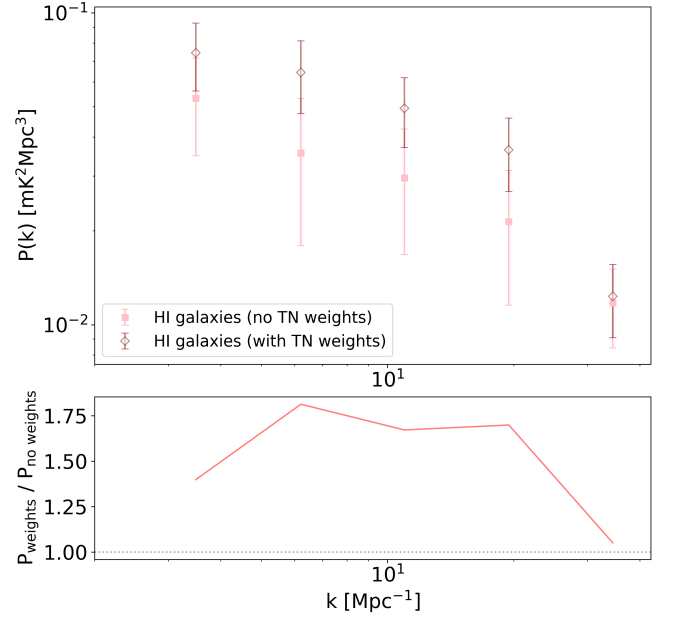


Figure 13. The $H\text{I}$ power spectrum on the $H\text{I}$ galaxies, comparing the cases of including and excluding the thermal noise weights when using the estimator.

windows must be applied to any model power spectrum for a proper comparison.

4.3 Estimating error bars based on M_{HI} uncertainties

The final step is to estimate an error on the power spectrum from these galaxies. So far, the error bars shown on the power spectra have been estimated using a Jackknife approach. We mask pixels containing individual galaxies in the mesh and run the entire power spectrum code end-to-end, from assigning $H\text{I}$ mass to the mesh to the power spectrum estimation. Due to the small sample of galaxies, this method and the sampling variance in Equation 4 do not capture the uncertainty in the power spectrum we are estimating, especially when we want to compare to the power spectrum estimated on the visibility data. The M_{HI} of these galaxies have an uncertainty associated with them according to the mass range in which they lie. These uncertainties are derived from the noise properties of the $H\text{I}$ cubes from which these galaxy masses are measured (Maddox et al. 2021), and a detailed description of these mass measurements is given in Ponomareva et al. (2023). The exact levels are given at the 5% level for $M_{\text{HI}} > 10^9 M_{\odot}$, 10% for $10^8 M_{\odot} < M_{\text{HI}} < 10^9 M_{\odot}$, and up to $\sim 20\%$ for $M_{\text{HI}} < 10^8 M_{\odot}$ (Ponomareva et al. 2021; Rajohnson et al. 2022; Ponomareva et al. 2023). To capture this uncertainty in the power spectrum error bars, this percentage-based criterion is used to create a distribution for each M_{HI} selected from the catalogue with a standard deviation, $\sigma_{M_{\text{HI}}}^i$ given as the percentage fraction of the individual $H\text{I}$ mass, M_{HI}^i , with a mean, $\mu_{M_{\text{HI}}}^i = M_{\text{HI}}^i$. We produce 10,000 random samples for the distribution of each galaxy, and a catalogue is created by randomly selecting a sample $H\text{I}$ mass for each galaxy and running the pipeline end-to-end to estimate a power spectrum for each catalogue of samples. The mean and standard deviation of these power spectrum realisations are the final estimates we compare to the power spectrum estimated on the visibility data using Equation 3 with errors given by Equation 4. These errors are the only source of uncertainty used when showcasing and comparing

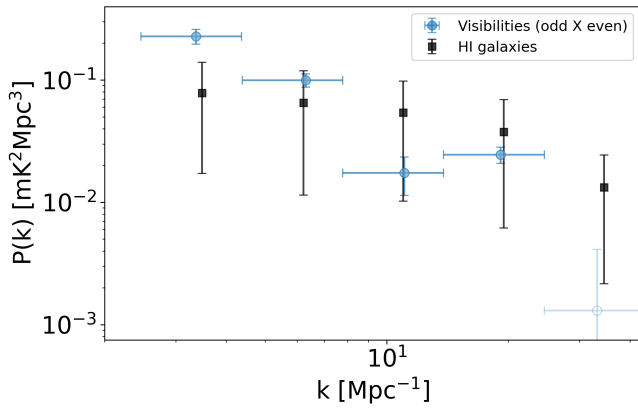


Figure 14. The comparison of the 1D power spectrum estimated on the "odd" \times "even" power spectrum obtained from the MIGHTEE visibility data (blue circles) to the power spectrum estimated on the detected H I galaxies (black squares). The 5σ flagging criterion was applied to both 3D power spectrum cubes before performing the spherical average to obtain these 1D power spectrum estimates. Both also make use of the inverse thermal noise variance weighting. The errors estimated on the H I galaxy case were generated using random sampling based on the uncertainties in the detected H I mass, while the errors estimated in the visibility power spectrum case use Equation 4. Negative power amplitudes are shown as shaded open circles and are also included with the corresponding effective k in Table 3.

the power spectrum estimated on the H I galaxies in the rest of this study.

4.4 Power Spectrum Comparison

The key result in this section is the comparison of the power spectrum estimated on the cross-correlated combined COSMOS visibility data and the power spectrum estimated on the detected H I galaxies using the same data set. This is shown in Figure 14. Since these power spectra use different data products from the same set of MIGHTEE observations on a single pointing, the expectation is that the comparison should be consistent within the error bars, where the error in the power spectrum measured on the visibilities comes from sampling variance, weighted by thermal noise simulations (inverse noise variance weighting), while for the power spectrum from the H I galaxies is sourced by the percentage uncertainties in the H I masses in the catalogue. Any residual contamination is also expected to contribute to the error bars of the cross-correlation visibility power spectrum estimate and would be a source of bias in this comparison (as discussed in Section 5.4). Furthermore, we do not expect cosmic variance or shot noise to account for the differences in the two power spectrum measurements, as they are both measured on the same field. However, uncertainties in the H I mass estimation can lead to noticeable differences. For the Early Science MIGHTEE galaxy catalogue, the W_{50} values are biased to smaller values and might not fully represent the velocity fields of all the galaxies on the COSMOS field accurately. Larger W_{50} values for these galaxies would further suppress the estimated power spectrum, which could explain the differences between the result from the H I galaxies and visibilities observed beyond $k = 10 \text{ Mpc}^{-1}$. It is also likely the case that the error bars on the H I galaxies are an overestimation since they are based on fixed percentage uncertainties in mass ranges, rather than uncertainties in the individual galaxy H I masses themselves. Nonetheless, the comparison of the power spectra estimates are consistent, with the

difference at about the 20% level, which is a possible indication that the error bars on the H I galaxy power spectrum might indeed be overestimated.

5 VALIDATIONS: H I POWER SPECTRUM FROM THE VISIBILITIES OF DETECTED H I GALAXIES

We further present tests by simulating a new visibility dataset from the detected MIGHTEE H I galaxies and processing it using exactly the same pipeline as the one used on the original MIGHTEE visibility dataset (Section 3). This would allow us to compare the signal levels and enable us to cross-correlate the two datasets, with the goal of testing that the visibilities and H I galaxy detections do correlate in position and frequency. Both thermal noise and systematics will not correlate with the high signal-to-noise detected galaxies. Such an approach would require a visibility simulator. The details of this simulator and the validation tests are discussed in the subsections that follow.

5.1 MeerKAT All-Sky Simulator (MASS)

MASS is a simulator that estimates visibilities from a radio interferometric experiment and outputs them in the standard measurement set format for analysis. Considering the problem at hand, our aim here is to simulate visibilities given the H I selected galaxy sky coordinates, redshifts, H I mass, and W_{50} . For this work, we have 37 such galaxies that host the H I. Here, we consider a simplified assumption that each galaxy subtends an angle that is much smaller than the resolution derived from the baseline range of our data. However, the velocity structure of the H I inside the individual galaxies is well within the frequency resolution of our interest. We include the frequency spread of the H I emission in the simulation by introducing a line profile $\phi_i(\nu = \nu_i)$ associated with each galaxy (i), where $\int \phi_i(\nu) d\nu = 1$. The line profile here has been defined with respect to the observed frequency in the rest frame of the telescope.

Visibilities corresponding to the galaxy distribution are calculated using,

$$\mathcal{V}(\mathbf{U}_n, \nu_a) = \left(\frac{\partial B}{\partial T} \right)_{\nu_a} \frac{1}{r^2 r'} \sum_i T_{\text{HI}}^i A(\theta_i, \nu_i) \phi(\nu_a - \nu_i) e^{2\pi i \mathbf{U}_n \cdot \theta_i}, \quad (15)$$

where $B = 2k_B T / \lambda^2$ is the Planck function in the Rayleigh-Jeans limit, which is valid in the frequency range of our interest ($\sim 1330 - 1390 \text{ MHz}$), and T_{HI}^i is the brightness temperature distribution from the i^{th} galaxy on the sky. The primary beam pattern for the telescope is given by $A(\theta, \nu)$, r is the comoving distance to the redshift (z_c) of the central frequency (ν_c) channel and $r' = |dr/d\nu|_{\nu_c}$. For this work, we have chosen a simple line profile,

$$\phi(\nu - \nu_i) = \begin{cases} \frac{1}{F_i \Delta \nu_c}, & \text{for } |\nu - \nu_i| \leq \frac{F_i}{2} \times \Delta \nu_c \\ 0, & \text{otherwise.} \end{cases} \quad (16)$$

Here, the value of F_i has been estimated from the measured W_{50} of each galaxy. Further details and results from using the H I detections as the sky input to MASS are discussed in Section 5.2.

Before doing so, we test the MASS pipeline on a realisation of the sky generated using a simple $P(k) = k^{-2}$ power law model as input. Visibilities are generated on this sky model and then put through the end-to-end pipeline and power spectrum estimator discussed in Section 3. The result of this is then compared to the theoretical k^{-2}

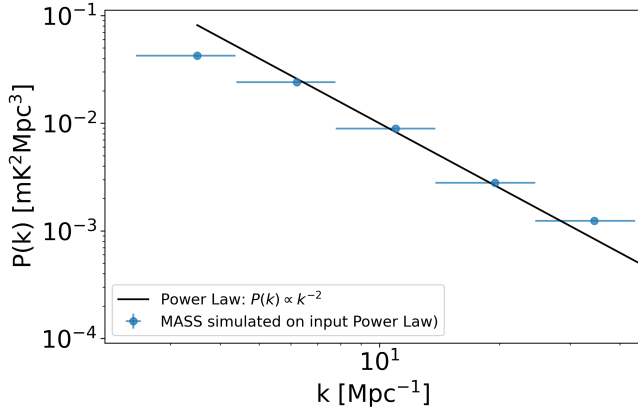


Figure 15. Comparison between an input power law H I power spectrum and a single realization of a sky model generated using this power law as input to generate MASS simulated visibilities. The difference between low and high k is due to the variance in this single realization, as it is randomly generated. Regardless, the two are in good agreement across the k range shown.

power law as shown in Figure 15. We find good agreement between the two power spectra. However, since this realisation is randomly generated, the variance will cause it to deviate from the theoretical model, which is what is observed at $k \sim 3 \text{ Mpc}^{-1}$ and $k \gtrsim 30 \text{ Mpc}^{-1}$. Thus, we confirm that MASS can accurately simulate the H I given an input.

5.2 Detected H I galaxies power spectrum comparison

To ensure that the end-to-end pipeline that generates the mesh and estimates the H I power spectrum on the detected H I galaxies from the catalogue is performing these processes correctly, we make use of MASS to test if we can recover the H I signal present in the detected H I galaxies. The input configuration for the baselines corresponds to that of the entire set of data blocks used in the analysis. In other words, we make use of the combined uv distribution of all the MIGHTEE visibility data to simulate with MASS. Since there is no thermal noise added to these particular runs of the simulations, as long as the uv coverage is comparable to the full uv coverage of the combined data blocks, we expect to be able to recover the signal with our estimator. Once the visibilities are generated using MASS, we apply the same procedures as is done to the MIGHTEE visibility data for gridding, forming the 3D power spectrum, and estimating the 1D power spectrum with its error bars. The same thermal noise weights used for the MIGHTEE data are applied as well in order to sample the 3D power spectrum in the same way. However, since these simulations only use H I signal to generate visibilities, the resulting 1D power spectra have negligible error bars. Like in the previous simulation, the main source of errors will be the catalogue H I mass. To simplify the analysis, we do not include this error here since it will not impact the validation tests.

The output cylindrical power spectrum is shown in Figure 16. We can clearly see the H I signal distributed over $(k_{\perp}, k_{\parallel})$. A lot of the power is close to the foreground wedge which indicates that flagging around that region might lead to signal loss when averaging to the 1D power spectrum

Figure 17 shows the spherically averaged 1D power spectrum in comparison to the one from the H I galaxy pipeline described in Section 4. The estimates are consistent up until $k \sim 42 \text{ Mpc}^{-1}$. This k limit corresponds to the resolution set initially to the H I temperature

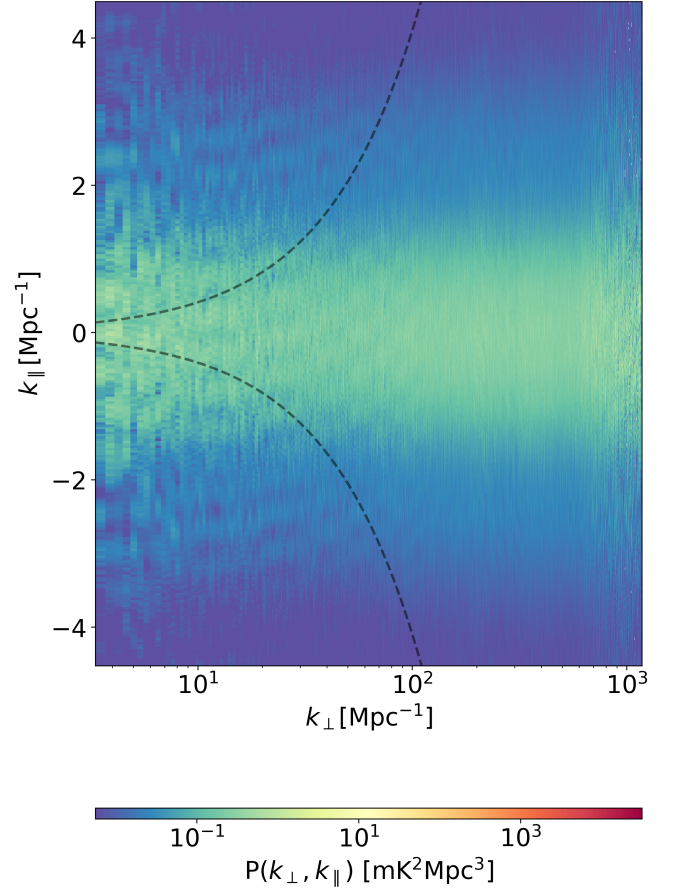


Figure 16. The cylindrical power spectrum estimated on the gridded delay-transformed visibilities generated using MASS. It uses the same information from the H I detections to produce this power spectrum.

cube, $k_{\max} = \pi/\Delta r_{\text{pix}}$, where Δr_{pix} is the pixel size of the cube that we set to $0.05 \text{ Mpc}/h$. For the comparison between the visibility power spectrum results in both auto- and cross-correlation, it is sufficient that the comparison is consistent below $k \sim 20 \text{ Mpc}^{-1}$, since the power spectrum estimated on the visibility data is noise-dominated beyond this k and we nonetheless do not expect to extract any meaningful information from the power spectrum at $k \gtrsim 20 \text{ Mpc}^{-1}$, as this will correspond to scales comparable to the physical sizes of galaxies. Overall, the consistency between the two results is an indication that the visibility gridding, averaging, and power spectrum estimation pipeline has a comparable output to the H I galaxy power spectrum produced on the H I detections.

5.3 Cross-correlating the MIGHTEE Gridded Visibilities with MASS

Another important way to test our pipeline, and the validity of our power spectrum estimates, is to do a cross-correlation between the delay-transformed gridded visibilities from the MIGHTEE data and those output from MASS. To do so, we use:

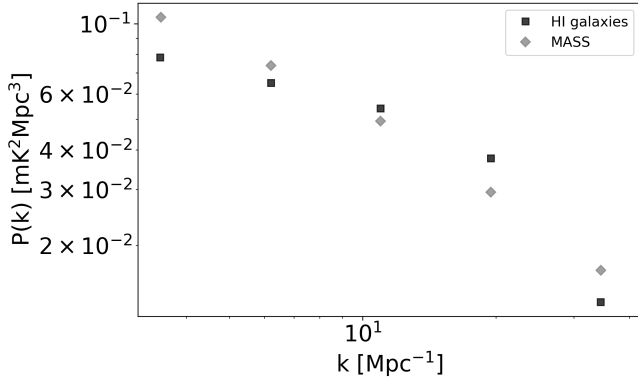


Figure 17. Comparison of the 1D power spectra generated using the pipeline described in Section 4 and using MASS. For each, there is no thermal noise present, and therefore, we expect the two results to be consistent. The deviations between the two are likely due to how many modes are averaged in each k bin to obtain the estimates, as well as differences in pre-processing steps, which introduce residual errors.

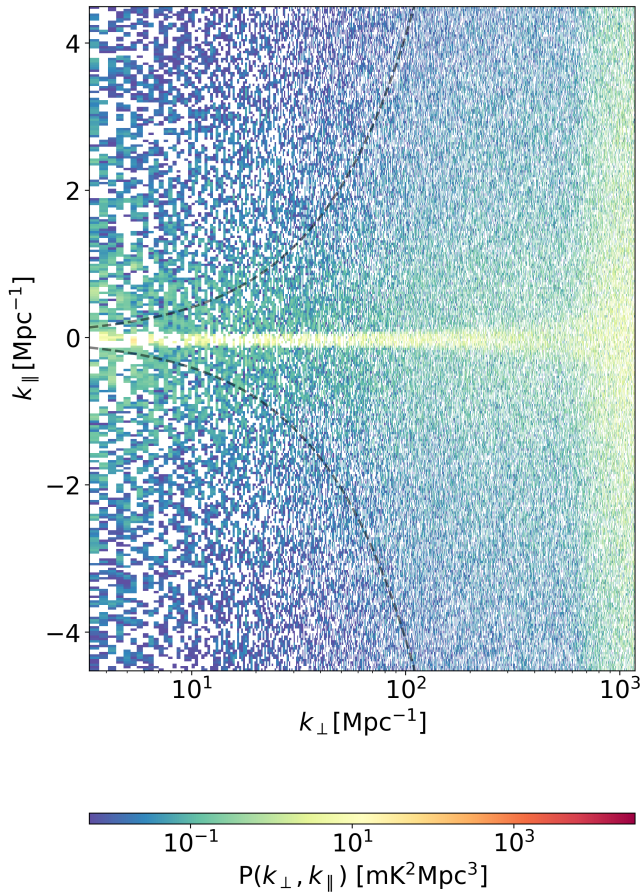


Figure 18. The cylindrical power spectrum of vis \times MASS, without any power spectrum flagging applied. Also shown is the horizon limit, $k_{\parallel}^{\text{horizon}}(k_{\perp})$ as a dashed grey line for $\pm k_{\parallel}$. Clearly seen here is the removal of the foreground wedge and contamination present in the MIGHTEE data. The H I present in both the visibility data and MASS is seen at low k_{\parallel} , and spread across k_{\perp} in a similar manner to that seen in Figure 16.

$$P_{\text{vis} \times \text{MASS}}(\mathbf{u}, \tau) = \frac{V_{\text{vis}}(\mathbf{u}, \tau)V_{\text{MASS}}^*(\mathbf{u}, \tau) + V_{\text{vis}}^*(\mathbf{u}, \tau)V_{\text{MASS}}(\mathbf{u}, \tau)}{2} \times \left[\left(\frac{\lambda^2}{2k_B} \right)^2 \frac{A_e}{\lambda^2 B} \frac{r_v^2 \Delta r_v}{B} \right], \quad (17)$$

where V_{vis} is the combined, gridded, averaged, and delay-transformed data from MIGHTEE and V_{MASS} is the delay-transformed gridded visibilities created on the MASS output using the H I detections from MIGHTEE as the input model with flux profiles assigned using a boxcar along frequency. The power spectrum estimators for cylindrical and spherical averaging in Equation 3 and Equation 5, respectively, are applied to this, applying the weights, $w = 1/\sigma_{P_{\text{TN}}}^2$, derived from the thermal noise simulations.

The cylindrical power spectrum of this cross-correlation is shown in Figure 18. No flagging at the 3D power spectrum level has been applied here. However, we can see that both noise, foregrounds and systematics have been mitigated in the cross-correlation, as expected. For instance, even inside the wedge, around $k_{\parallel} = 0$, most power amplitude pixels are removed. Comparing this to 16, we can identify the region where the H I power is dominating. After the horizon cut, most of the signal will still be close to the wedge and at low k_{\perp} . Note, however, that we do not expect a perfect correlation between the data visibility H I signal and the MASS-generated H I visibilities. Small differences in the phases of the complex numbers in Equation 17 will inevitably lead to decorrelation. In practice, besides numerical issues, there are a few possibilities for a mismatch in the two H I signals: 1) there could be more H I than that detected in the high signal to noise galaxies; 2) we might be resolving the low redshift galaxies (assumed to be point sources in the MASS simulation); 3) the H I line profile might be different (we are assuming a Boxcar distribution using the W_{50} values) and 4) there could be a mismatch between the galaxy redshifts (which translates to a mismatch in the frequencies).

In Figure 19 we compare the auto power spectrum of the MASS visibilities to the power spectrum from our original MIGHTEE Stokes I visibilities (cross power of odd \times even), after the 5σ flagging. Included as well is the cross-power from Equation 17, between MASS and the total (odd + even) Stokes I visibilities (without any 5σ flagging). The power of the MASS autocorrelation is quite close to our visibility cross-power, indicating that most of the H I should be in the detected galaxies, and our 5σ flagging is removing most of the contamination without incurring significant signal loss. On the other hand, the cross between MASS and visibility data shows a significant drop, as expected, due to a probable phase mismatch. We tested slightly moving the galaxy redshifts in a random way without any noticeable change in this cross power. The most likely culprit, at least at low k_{\perp} , should be point 3) above (different line profiles). Many actual H I galaxy profiles would be closer to either Gaussian-shaped or exhibit a double-horn feature, meaning that there will be cases where the shapes and extents of the galaxies along frequency are quite different. Another difference, which can be noticeable but has a smaller impact, would be the beam correction. The beam correction for MASS outputs is calculated at the higher end of the bandwidth, i.e., at ~ 1392 MHz, while for the visibility data, the beam correction has been calculated at the centre of the band, ~ 1362 MHz. This is an approximately 30 MHz shift between beam correction calculations for each case.

To further confirm that the measured cross-correlation signal between MASS and data visibilities is real, we have run another test,

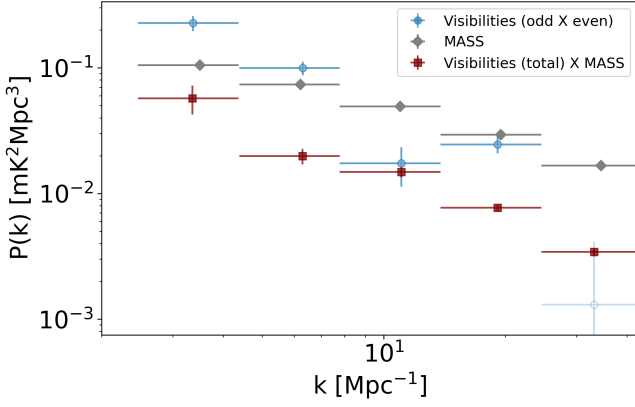


Figure 19. The 1D power spectrum of vis \times MASS compared to the power spectrum of the MASS-generated gridded visibilities, and the cross-power (odd \times even) Stokes I of the MIGHTEE visibility data after applying the 5σ cut.

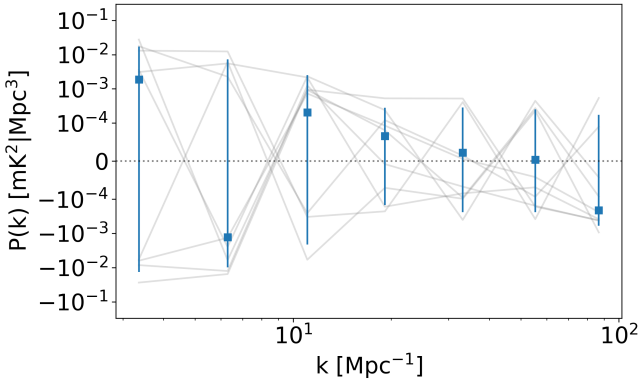


Figure 20. The mean and standard error over 9 realisations of the 1D power spectrum formed from the visibilities cross-correlated with the shuffled MASS realisations. Also shown are the individual cross power spectra for each realisation in grey.

where we randomly shuffled the $H\text{I}$ detections along the line-of-sight and used this as input in the MASS pipeline to generate visibilities with which to cross-correlate the MIGHTEE data. The procedure is essentially the same as that described in Section 5.3. If we indeed see a valid signal in this cross-correlation (see Figure 19), a reshuffling of the positions of galaxies would result in a decorrelation, thus making the result of this new cross-correlation consistent with zero.

The new galaxy positions are completely random along each of the axes (R.A., Dec., z) of the volume that contains these galaxies. Due to computational limitations, this is only done for 9 realisations of this random placement of galaxies. The resulting 9 measurement sets are then gridded using the visibility pipeline. These gridded outputs are then crossed with the gridded MIGHTEE visibility data using Equation 17. The subsequent power spectra estimated on these are averaged and shown in Figure 20 with the standard deviation of the 1D power spectrum realisations used as the error in each k bin. Indeed, we find that with a selection of randomly shuffled $H\text{I}$ galaxy sky models, there is negligible correlation with the visibility data when compared to cross-correlating the actual MIGHTEE detected $H\text{I}$ galaxies with the visibility data.

5.4 Signal loss

We now study the impact of the 3D gridded visibility power spectrum flagging on signal loss with the aid of the MASS simulation. We start by considering two more cases: 9σ and 3σ , and compare them to the standard 5σ flagging we use for the main results in this study. The 9σ should still remove significant contamination while mitigating some of the signal loss that inevitably results from having to remove increasingly more k modes from the 3D power spectrum cube. The 3σ case is the least conservative cut that can be considered before considerable portions of the modes available in the k bins are flagged away, resulting in larger signal loss in our power spectrum estimates.

Figure 21 shows the flagging fraction projected on the uv plane for the 9σ and 3σ cases. As in the case of 5σ shown in Figure 7, the highest flagging fractions are confined within a region $\sim \pm 1.825 k\lambda$. Beyond this, most of the flagged points on the uv grid will be thermal noise, and therefore appear random in this centralised portion of the uv distribution shown. This is justified when looking at the flagging fraction for the 9σ case, which, similarly to the 5σ case, removes the bright contamination that appears to have stripe-like features, but has a reduced flagging fraction beyond $\sim \pm 1.825 k\lambda$ since there is less thermal noise being removed by this level of flagging as compared to 3σ . Despite this, even at the 9σ level, the centrally-confined contamination, which appears localised in the cylindrical power spectra, is flagged out by this criterion. On the other hand, the 3σ case removes the modes similarly to that seen at the 5σ level, but has a noticeably higher flag fraction across the uv distribution. On average, there is about a 10-15% of uv modes flagged in comparison to $\sim 5\%$ for the 5σ case.

Figure 22 shows the ratios of the 2D cylindrical auto power spectra for the different σ flag cases with respect to the no flagging case. We remind again that flagging is done at the 3D power spectra level. We see that the 9σ level already picks up the main contaminants. As the flagging increases, there will be more pixels with the power reduced as expected. However, this could simply be due to noise outliers or even stronger $H\text{I}$ power. Note that flagging noise outliers should not bias the cross-power between the "even" and "odd" datasets. For 3σ , the flagging becomes more aggressive, but still is mainly restricted to removing the strong contamination at $k_{\perp} \lesssim 10 \text{ Mpc}^{-1}$ and $k_{\parallel} \lesssim 1 \text{ Mpc}^{-1}$. These results also translate to the 1D power spectrum estimates for each case as seen in Figure 23 (odd \times even power spectra). We can see that there is a clear drop from the case with no contamination flagging to the 9σ case, especially for the second and third bins. Interestingly, the drop from 9σ to 5σ is much smaller, indicating that most of the contamination is already picked up by the 9σ flagging. At the same time, we see a continuous drop in power from 9σ to 3σ . There could be two reasons for this: either we are still removing contamination (that correlates between the odd and even datasets), or we have signal loss.

Applying the same 3D (k_{\perp} , k_{\parallel}) cube masks to the MASS simulation should help us understand this better. Figure 24 shows the results for the 9σ , 5σ and 3σ cases. The top panel shows the 1D power spectra estimated on the MASS-generated, gridded visibilities, while the bottom panel shows the ratio of each σ cut case to the case where no cut is applied. Although there is a consistent signal drop, this is smaller than what is observed for the original signal in Figure 23. A similarly small drop in the signal was observed in Section 4.2 where the 5σ flags were tested $H\text{I}$ galaxies placed in a cosmological volume. This is probably an indication that there is more power in the original $H\text{I}$ signal closer to the wedge, where most of the flagging is being applied (Figure 22). This should not be a complete surprise, as we have seen that the cross-correlation of the original visibility data

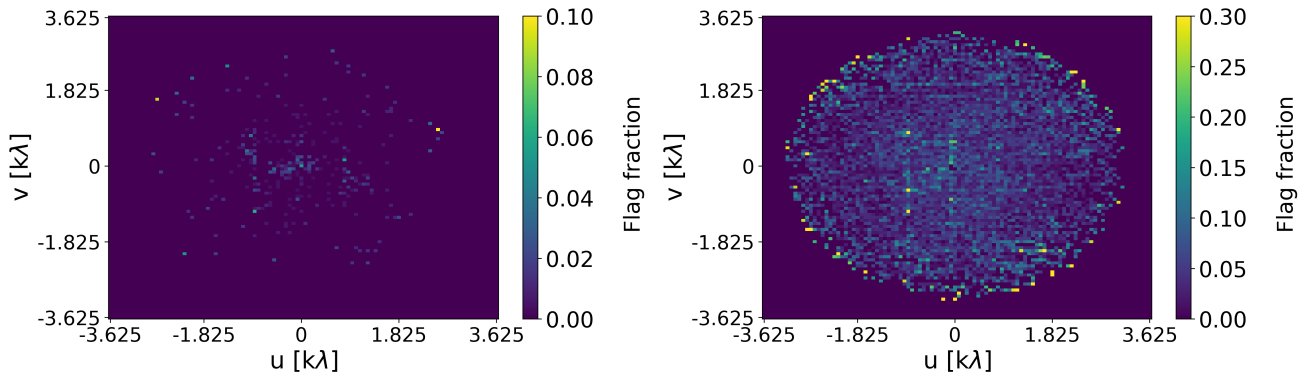


Figure 21. The flagging fraction when we apply 9σ (left) and 3σ (right) level flags to the 3D visibility power spectrum cube within the estimation window. In the 3σ case, the flag fraction is a lot more pronounced throughout the uv grid as the flagging is more aggressive compared to the 9σ case. Even so, the localized contamination in the centre of the uv distribution is still flagged on close inspection of this 9σ case.

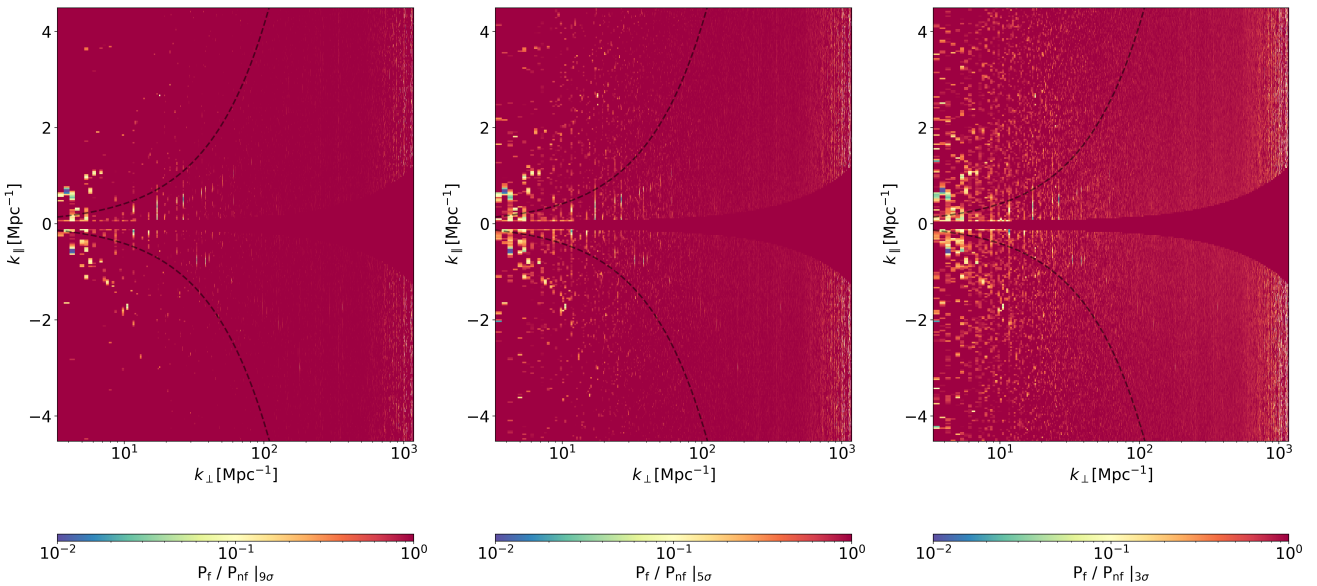


Figure 22. The ratio of the cylindrical power after performing 9σ (left), 5σ (middle), and 3σ (right) flagging to the cylindrical power spectrum without any flagging applied. The smaller foreground-dominated region inside the wedge is not flagged for any of the cases since we want to assess the level of spillover and contamination near and around this region itself. The ratios shown here help demonstrate the level of flagging done within the estimation window for each case and along k_{\perp} as the thermal noise level increases, which is particularly pronounced for 3σ , as we expect this to flag a larger portion of noise-dominated k pixels in comparison to the other cases.

with the MASS output shows some decorrelation. Therefore, a final test would be to check the impact of the flags on the cross-correlation between the data and MASS visibilities.

The cross-correlation with the MASS simulation derived from detected galaxies should be free of contamination. If the drop in power in the data as we go from 9σ to 3σ flagging is only due to the removal of contaminants, we should not see that effect in the cross-correlation since the systematics will not correlate. Figure 25 shows the impact of flagging on this cross-power spectrum. Note that the same flags are applied to the delay transformed visibility cube before calculating the cross-power. Clearly we see a drop in power larger than in Figure 24. This is probably an indication that more H I is being removed in the original visibility dataset than what is seen in the MASS simulation. The bottom panel of Figure 25 shows a signal loss below 20% for the 5σ case, dropping to 30% in the 3σ case. Therefore, although the level of contamination after the sigma

flagging is expected to be low, some care must be taken with signal loss.

6 CONCLUSIONS

In this work, we have investigated the feasibility of measuring the H I intensity mapping signal at low redshifts ($z \approx 0.04$) using interferometric observations from the central pointing of the MIGHTEE COSMOS field. With ~ 17.5 hours of MIGHTEE data and a delay-spectrum-based power spectrum estimator, we have measured the H I power spectrum on sub-megaparsec scales over the frequency range 1332 - 1392 MHz. This analysis extends previous MeerKAT interferometric intensity mapping studies to a regime at lower redshifts where individual H I galaxy detections are available within the same dataset, enabling a direct and self-consistent validation of the methodology.

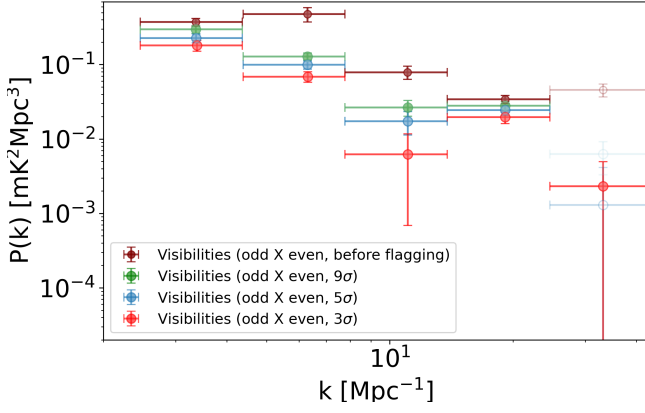


Figure 23. The $H\text{I}$ power spectrum estimates for the cases of 3, 5, and 9σ flagging levels compared to the case where no σ flagging has been performed. Negative amplitudes are shown as open, shaded circles with the associated error bars. Beyond $k \sim 20 \text{ Mpc}^{-1}$, thermal noise is expected to dominate.

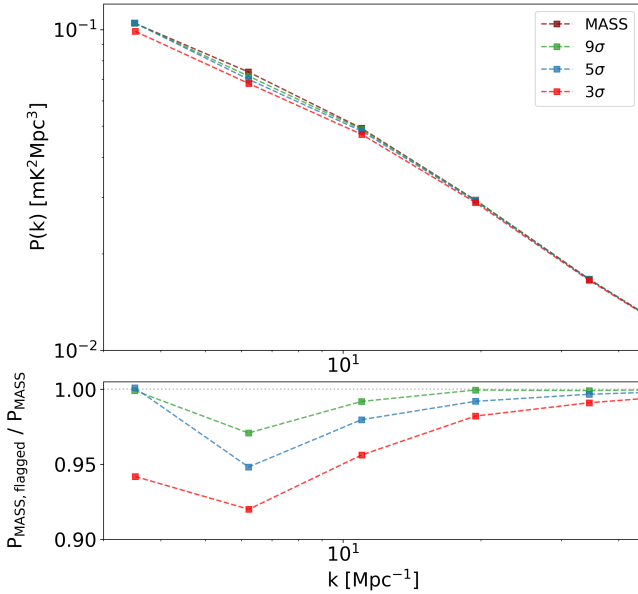


Figure 24. The top panel shows the 1D $H\text{I}$ power spectrum estimated on the MASS-generated visibilities using the $H\text{I}$ galaxy detections as input compared to the 9, 5 and 3σ cut power spectra cases. The bottom panel shows the ratios of each of these σ cut cases to the case where no σ cut is applied.

As in previous MeerKAT intensity mapping analyses, we identify low-level broadband contamination in the power spectrum, primarily localised at low k_{\perp} and close to the foreground wedge. This contamination is visible in both auto- and cross-power spectra at the cylindrical power spectrum level and is consistent with residual systematics rather than thermal noise. Following the approach adopted in earlier work (Paul et al. 2023), we mitigate this effect by flagging strong outliers directly at the three-dimensional power spectrum (or delay transformed visibility) level using detailed thermal noise simulations. The fraction of flagged voxels is small, typically in the range $\sim 2 - 5\%$, and therefore expected to have a limited impact on the cosmological signal. After applying a conservative 5σ cut, the one-dimensional power spectrum obtained from cross-

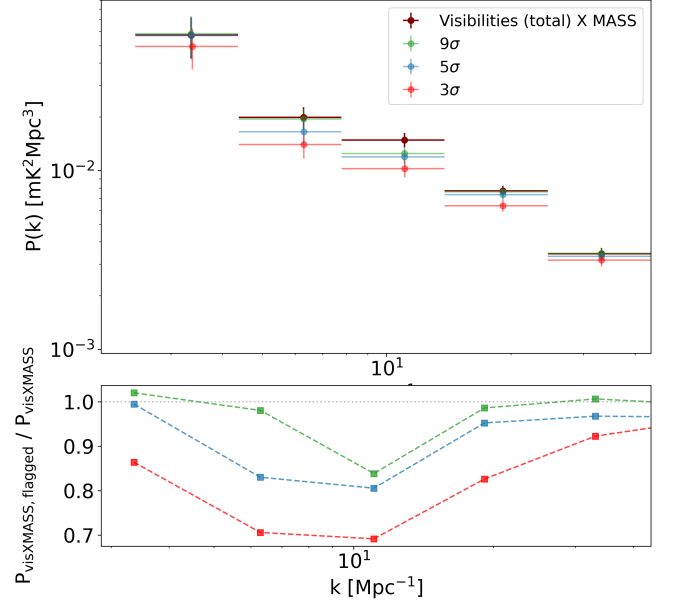


Figure 25. The $\text{vis} \times \text{MASS}$ power spectrum compared to the results obtained from applying 9, 5, and 3σ cuts shown in the top panel. The bottom panel shows the ratio of these σ cut cases to the case where no σ flagging is applied.

correlating visibilities split in time exhibits a signal that appears free from detectable contamination. The total signal-to-noise ratio of this cross-power spectrum measurement is approximately 13.

A key objective of this study has been to validate the full end-to-end power spectrum pipeline using the detected $H\text{I}$ galaxies in the MIGHTEE COSMOS field. This validation was carried out in two complementary ways. First, the measured $H\text{I}$ masses were directly distributed into a comoving intensity field, from which a power spectrum was estimated using the same gridding and averaging procedures. Second, the detected galaxies were used as inputs to the MeerKAT All-Sky Simulator (MASS) to generate synthetic visibilities, which were then processed through the full visibility-based pipeline. In both cases, the recovered power spectra are consistent with the visibility-based measurements up to $k \sim 20 \text{ Mpc}^{-1}$, beyond which the measurements become noise-dominated and no meaningful constraints are expected. This agreement provides a strong internal consistency check on the gridding, delay transform, weighting, and power spectrum estimation steps of the pipeline.

We further tested the astrophysical origin of the measured signal through cross-correlations between the observed visibilities and MASS-generated visibilities. A statistically significant correlation is observed when using the true galaxy distribution, while randomised galaxy realisations yield null results. These tests demonstrate that the measured signal is associated with the $H\text{I}$ galaxy population rather than residual systematics or noise fluctuations. Differences between the auto- and cross-correlations involving simulated visibilities are consistent with expected effects arising from simplified assumptions in the simulations, such as idealised line profiles and beam modelling. However, the simulations indicate that a non-negligible fraction of the $H\text{I}$ power lies close to the wedge, implying that aggressive flagging can lead to measurable signal suppression. This highlights the need for careful, simulation-calibrated treatments of foreground mitigation when interpreting one-dimensional power spectra, particularly

at low redshift where the H I signal is strongly anisotropic in $(k_{\parallel}, k_{\perp})$ space.

Overall, this work demonstrates that interferometric H I intensity mapping with MeerKAT can recover a power spectrum that is consistent, within uncertainties, with that inferred from directly-detected H I galaxies in the same field over the range of scales where the measurement is signal-dominated. While the present dataset does not allow for a precision cosmological measurement, the combination of internal null tests, contamination mitigation, and end-to-end validation provides strong evidence that the recovered signal is robust and astrophysical in origin.

ACKNOWLEDGEMENTS

JT and MGS acknowledge support from the South African Radio Astronomy Observatory and National Research Foundation (Grant No. 84156). SC acknowledges financial support from the South African National Research Foundation (Grant No. 84156) and the Inter-University Institute for Data Intensive Astronomy (IDIA). IDIA is a partnership of the University of Cape Town, the University of Pretoria and the University of the Western Cape. IDIA is registered on the Research Organization Registry with ROR ID 01edhwb26, and on Open Funder Registry with funder ID 100031500. The authors acknowledge the use of the ilifu cloud computing facility – www.ilifu.ac.za, a partnership between the University of Cape Town, the University of the Western Cape, Stellenbosch University, Sol Plaatje University and the Cape Peninsula University of Technology. The ilifu facility is supported by contributions from IDIA, the Computational Biology division at UCT, and the Data Intensive Research Initiative of South Africa (DIRISA).

DATA AVAILABILITY

The data and simulation outputs underlying this article will be shared upon reasonable requests.

REFERENCES

Anderson C. J., et al., 2018, *Monthly Notices of the Royal Astronomical Society*, 476, 3382

Baker A. J., Blyth S., Holwerda B. W., Team L., 2018, in *American Astronomical Society Meeting Abstracts #231*. p. 231.07

Barry N., Hazelton B., Sullivan I., Morales M. F., Pober J. C., 2016, *Monthly Notices of the Royal Astronomical Society*, 461, 3135

Battye R. A., Davies R. D., Weller J., 2004, *Monthly Notices of the Royal Astronomical Society*, 355, 1339

Bharadwaj S., Sethi S. K., 2001, *Journal of Astrophysics and Astronomy*, 22, 293

Bharadwaj S., Nath B. B., Sethi S. K., 2001, *Journal of Astrophysics and Astronomy*, 22, 21

Bull P., Ferreira P. G., Patel P., Santos M. G., 2015, *Astrophysical Journal*, 803, 1

CHIME Collaboration et al., 2022, *ApJS*, 261, 29

CHIME Collaboration et al., 2023, *The Astrophysical Journal*, 947, 16

Campbell D. B., 2002, in Stanimirovic S., Altschuler D., Goldsmith P., Salter C., eds, *Astronomical Society of the Pacific Conference Series Vol. 278, Single-Dish Radio Astronomy: Techniques and Applications*. pp 81–90

Chang T. C., Pen U. L., Peterson J. B., McDonald P., 2008, *Physical Review Letters*, 100, 1

Chang T., Pen U., et al. Bandura K., 2010, *Nature*, pp 463–465

Chen Z., Wolz L., Spinelli M., Murray S. G., 2021, *Monthly Notices of the Royal Astronomical Society*, 502, 5259

Chen Z., Wolz L., Battye R., 2022, *Monthly Notices of the Royal Astronomical Society*, 20, 1

Chen Z., Chapman E., Wolz L., Mazumder A., 2023, *Monthly Notices of the Royal Astronomical Society*, 524, 3724

Colombi S., Jaffe A., Novikov D., Pichon C., 2009, *MNRAS*, 393, 511

Cui W., Liu L., Yang X., Wang Y., Feng L., Springel V., 2008, *The Astrophysical Journal*, 687, 738

Cunnington S., Wolz L., 2024, *MNRAS*, 528, 5586

Cunnington S., et al., 2022, *Monthly Notices of the Royal Astronomical Society*

Datta A., Bowman J. D., Carilli C. L., 2010, *Astrophysical Journal*, 724, 526

Davé R., Anglés-Alcázar D., Narayanan D., Li Q., Rafieferantsoa M. H., Appleby S., 2019, *Monthly Notices of the Royal Astronomical Society*, 486, 2827

Deboer D. R., et al., 2017, *Publications of the Astronomical Society of the Pacific*, 129

Dodelson S., 2003, *Modern cosmology*. Academic Press, <https://cds.cern.ch/record/1282338>

Ewen H., Purcell E., 1951, *Nature*, 168

Furlanetto S. R., Oh S. P., Briggs F. H., 2006, *Phys. Rep.*, 433, 181

HERA Collaboration et al., 2022, *ApJ*, 925, 221

Hale C. L., et al., 2025, *MNRAS*, 536, 2187

Hand N., Feng Y., Beutler F., Li Y., Modi C., Seljak U., Slepian Z., 2018, *The Astronomical Journal*, 156, 160

Heywood I., et al., 2021, *Monthly Notices of the Royal Astronomical Society*

Heywood I., et al., 2024, *MNRAS*, 534, 76

Huang S., Haynes M. P., Giovanelli R., Brinchmann J., 2012, *ApJ*, 756, 113

Jarvis M. J., et al., 2016, *Proceedings of Science*, pp 25–27

Jing Y. P., 2005, *The Astrophysical Journal*, 620, 559

Kovetz E. D., et al., 2017, *arXiv e-prints*

Li Z., Wolz L., Guo H., Cunnington S., Mao Y., 2024, *Monthly Notices of the Royal Astronomical Society*, 534, 1

Liu A., Shaw J. R., 2020, *Publications of the Astronomical Society of the Pacific*, 132

Liu A., Parsons A. R., Trott C. M., 2014, *Physical Review D - Particles, Fields, Gravitation and Cosmology*, 90

Maddox N., Hess K. M., Obreschkow D., Jarvis M. J., Blyth S.-L., 2015, *MNRAS*, 447, 1610

Maddox N., et al., 2021, *A&A*, 646, A35

Masui K. W., et al., 2013, *Astrophysical Journal Letters*, 763

Mauch T., et al., 2020, *The Astrophysical Journal*, 888, 61

Mazumder A., et al., 2025, *MNRAS*, 541, 476

McQuinn M., Zahn O., Zaldarriaga M., Hernquist L., Furlanetto S. R., 2006, *The Astrophysical Journal*, 653, 815

MeerKLASS Collaboration et al., 2025, *MNRAS*, 537, 3632

Meyer M., Robotham A., Obreschkow D., Westmeier T., Duffy A. R., Staveley-Smith L., 2017, *Publ. Astron. Soc. Australia*, 34, 52

Morales M. F., 2005, *The Astrophysical Journal*, 619, 678

Morales M. F., Hewitt J., 2004, *The Astrophysical Journal*, 615, 7

Morales M. F., Beardsley A., Pober J., Barry N., Hazelton B., Jacobs D., Sullivan I., 2019, *Monthly Notices of the Royal Astronomical Society*, 483, 2207

Newburgh L. B., et al., 2016, in Hall H. J., Gilmozzi R., Marshall H. K., eds, *Society of Photo-Optical Instrumentation Engineers (SPIE) Conference Series Vol. 9906, Ground-based and Airborne Telescopes VI*. p. 99065X ([arXiv:1607.02059](https://arxiv.org/abs/1607.02059)), doi:10.1117/12.2234286

Pan H., et al., 2022, *Monthly Notices of the Royal Astronomical Society*

Parsons A., Pober J., McQuinn M., Jacobs D., Aguirre J., 2012a, *Astrophysical Journal*, 753

Parsons A. R., Pober J. C., Aguirre J. E., Carilli C. L., Jacobs D. C., Moore D. F., 2012b, *Astrophysical Journal*, 756

Parsons A. R., et al., 2014, *Astrophysical Journal*, 788

Paul S., et al., 2016, *Astrophysical Journal*, 833, 213

Paul S., Santos M. G., Townsend J., Jarvis M. J., Maddox N., Collier J. D., Frank B. S., Taylor R., 2021, *Monthly Notices of the Royal Astronomical Society*, 505, 2039

Paul S., Santos M. G., Chen Z., Wolz L., 2023, *arXiv e-prints*, p. [arXiv:2301.11943](https://arxiv.org/abs/2301.11943)

- Peacock J. A., 2003, *Philosophical Transactions of the Royal Society A: Mathematical, Physical and Engineering Sciences*, 361, 2479
- Planck Collaboration et al., 2020, *Astronomy and Astrophysics*, 641
- Pober J. C., et al., 2013, *Astrophysical Journal Letters*, 768
- Ponomareva A. A., et al., 2021, *MNRAS*, 508, 1195
- Ponomareva A. A., et al., 2023, *Monthly Notices of the Royal Astronomical Society*
- Pritchard J. R., Loeb A., 2012, *Rept. Prog. Phys.*, 75, 86901
- Rajohnson S. H., et al., 2022, *Monthly Notices of the Royal Astronomical Society*, 512, 2697
- Santos M. G., Cooray A., 2006, *Phys. Rev. D*, 74, 083517
- Santos M., et al., 2015a, in *Advancing Astrophysics with the Square Kilometre Array*. p. 19, doi:10.22323/1.215.0019
- Santos M., et al., 2015b, in *Advancing Astrophysics with the Square Kilometre Array (AASKA14)*. p. 19 (arXiv:1501.03989), doi:10.22323/1.215.0019
- Serra P., et al., 2015, *MNRAS*, 448, 1922
- Spinelli M., Zoldan A., de Lucia G., Xie L., Viel M., 2021a, *Monthly Notices of the Royal Astronomical Society*, 493, 5434
- Spinelli M., Carucci I. P., Cunnington S., Harper S. E., Irfan M. O., Fonseca J., Pourtsidou A., Wolz L., 2021b, *Monthly Notices of the Royal Astronomical Society*, 509, 2048
- Switzer E. R., et al., 2013, *Monthly Notices of the Royal Astronomical Society: Letters*, 434
- Taylor A. R., et al., 2024, *MNRAS*, 528, 2511
- Thyagarajan N., et al., 2013, *Astrophysical Journal*, 776
- Thyagarajan N., et al., 2015, *Astrophysical Journal*, 804
- Tudorache M. N., et al., 2022, *Monthly Notices of the Royal Astronomical Society*, 513, 2168
- Villaescusa-Navarro F., Viel M., Datta K. K., Choudhury T. R., 2014, *Journal of Cosmology and Astroparticle Physics*, 2014
- Wolz L., Tonini C., Blake C., Wyithe J. S., 2016, *Monthly Notices of the Royal Astronomical Society*, 458, 3399
- Wolz L., Blake C., Wyithe J. S. B., 2017, *Monthly Notices of the Royal Astronomical Society*, 470, 3220
- Wolz L., et al., 2021, *Monthly Notices of the Royal Astronomical Society*
- Wyithe J. S. B., Loeb A., 2009, *Monthly Notices of the Royal Astronomical Society*, 397, 1926
- van de Hulst H., 1945, *Ned. Tijdschr. Natuurk.*, pp 210–221

APPENDIX A: THE H I SHOT NOISE POWER SPECTRUM ON A SET OF H I GALAXIES

The derivation of the model of the expected H I shot noise power spectrum is showcased here. This model is useful as it allows us to directly compare the results from the H I galaxy catalogue to a model depending only on the H I mass in the catalogue and the average H I temperature in the given cosmological volume, as will be seen below. The derivation is based on the formalism outlined in (Wolz et al. 2016) and extended in (Chen et al. 2022). Start by defining the Fourier convention:

$$\tilde{f}(\mathbf{k}) = \int \frac{d^3\mathbf{x}}{V} f(\mathbf{x}) e^{i\mathbf{k}\cdot\mathbf{x}}, \quad (\text{A1})$$

and

$$f(\mathbf{k}) = \frac{V}{(2\pi)^3} \int d^3\mathbf{k} \tilde{f}(\mathbf{k}) e^{-i\mathbf{k}\cdot\mathbf{x}}, \quad (\text{A2})$$

with

$$\int \frac{d^3\mathbf{x}}{V} \delta_D^3(\mathbf{x} - \mathbf{x}') f(\mathbf{x}) = f(\mathbf{x}'), \quad (\text{A3})$$

where δ_D^3 is the Dirac delta function in three dimensions. The H I temperature at a given position, \mathbf{x} , can be expressed as

$$T_{\text{HI}}(\mathbf{x}) = C_{\text{HI}} \rho_{\text{HI}}(\mathbf{x}), \quad (\text{A4})$$

with the H I density is given by

$$\rho_{\text{HI}} = \frac{1}{V} \sum_i M_{\text{HI}}^i \delta_D^3(\mathbf{x} - \mathbf{x}'), \quad (\text{A5})$$

where i iterates over the H I sources in the given cosmological volume, V . C_{HI} is a multiplicative term that depends on redshift, z , which converts this H I density to temperature, and is given in Chen et al. (2022) as

$$C_{\text{HI}}(z) = \frac{3A_{12}h_{\text{pc}}^3(1+z)^2}{32\pi m_{\text{H}}k_{\text{B}}v_{21}^2 H(z)}. \quad (\text{A6})$$

In A5, ρ_{HI} is explicitly expressed in terms of the H I mass, M_{HI} , in the considered spatial volume, V . Here it is assumed that all the H I is contained in discrete sources over a relatively small spatial volume, i.e., that the H I content in the considered spatial volume is contained entirely within galaxies. Further, the H I temperature can also be expressed as

$$\begin{aligned} T_{\text{HI}}(\mathbf{x}) &= C_{\text{HI}} \rho_{\text{HI}}(\mathbf{x}) \\ &= \frac{C_{\text{HI}}}{V} \sum_i M_{\text{HI}}^i \delta_D^3(\mathbf{x} - \mathbf{x}'), \end{aligned} \quad (\text{A7})$$

so that the Fourier transform becomes

$$\begin{aligned} \tilde{T}(\mathbf{k}) &= \int \frac{d^3\mathbf{x}}{V} T_{\text{HI}}(\mathbf{x}) e^{-i\mathbf{k}\cdot\mathbf{x}} \\ &= \frac{C_{\text{HI}}}{V} \int \frac{d^3\mathbf{x}}{V} \sum_i M_{\text{HI}}^i \delta_D^3(\mathbf{x} - \mathbf{x}') e^{-i\mathbf{k}\cdot\mathbf{x}} \\ &= \frac{C_{\text{HI}}}{V} \int \frac{d^3\mathbf{x}}{V} \delta_D^3(\mathbf{x} - \mathbf{x}') \left[\sum_i M_{\text{HI}}^i e^{-i\mathbf{k}\cdot\mathbf{x}} \right] \\ &= \frac{C_{\text{HI}}}{V} \sum_i M_{\text{HI}}^i e^{-i\mathbf{k}\cdot\mathbf{x}_i}. \end{aligned} \quad (\text{A8})$$

With the form given for the Fourier-transformed H I temperature in Equation A8, the H I power spectrum can be written out in the form

$$\begin{aligned} P(\mathbf{k}) &= V \tilde{T}(\mathbf{k}) \tilde{T}^*(\mathbf{k}) \\ &= V \frac{C_{\text{HI}}^2}{V^2} \sum_i M_{\text{HI}}^i e^{-i\mathbf{k}\cdot\mathbf{x}_i} \sum_j M_{\text{HI}}^j e^{-i\mathbf{k}\cdot\mathbf{x}_j} \\ &= V \frac{C_{\text{HI}}^2}{V^2} \sum_{ij} M_{\text{HI}}^i M_{\text{HI}}^j e^{-i\mathbf{k}\cdot(\mathbf{x}_i - \mathbf{x}_j)}. \end{aligned} \quad (\text{A9})$$

Now consider the conditions for Equation A9 when the shot noise term dominates. Equation A9 is essentially a weighted average of galaxy pair counts done over ij for each galaxy pair. This equation is valid for all \mathbf{k} . However, in this case, we are looking for the limit in which $P(\mathbf{k})$ becomes constant for \mathbf{k} , i.e., the shot noise limit of the H I power spectrum expression. The shot noise originates from the discrete, noise-like nature of the distribution of H I sources. Hence, we are looking at the self-pairing component of Equation A9, i.e., when $i = j$. We, therefore have:

$$\begin{aligned}
P_{\text{H I}}^{\text{SN}} &= P_{\text{H I}}(\mathbf{k})|_{i=j} \\
&= \frac{C_{\text{H I}}^2}{V^2} V \sum_i (M_{\text{H I}}^i)^2 \\
&= \frac{C_{\text{H I}}^2}{V} \sum_i (M_{\text{H I}}^i)^2.
\end{aligned} \tag{A10}$$

The shot noise can be written in terms of the average H I temperature, given by

$$\begin{aligned}
\bar{T}_{\text{H I}} &= \int \frac{d^3\mathbf{x}}{V} T_{\text{H I}}(\mathbf{x}) \\
&= \int \frac{d^3\mathbf{x}}{V} \frac{C_{\text{H I}}}{V} \sum_i M_{\text{H I}}^i \delta_{\text{D}}^3(\mathbf{x} - \mathbf{x}') \\
&= \frac{C_{\text{H I}}}{V} \sum_i M_{\text{H I}}^i \int \frac{d^3\mathbf{x}}{V} \delta_{\text{D}}^3(\mathbf{x} - \mathbf{x}') \\
&= \frac{C_{\text{H I}}}{V} \sum_i M_{\text{H I}}^i.
\end{aligned} \tag{A11}$$

Therefore,

$$\bar{T}^2 = \frac{C_{\text{H I}}^2}{V^2} \left(\sum_i M_{\text{H I}}^i \right)^2, \tag{A12}$$

which implies that

$$C_{\text{H I}}^2 = \bar{T}^2 V^2 / \left(\sum_i M_{\text{H I}}^i \right)^2. \tag{A13}$$

Substituting Equation A13 into A10, the shot noise can therefore be rewritten as

$$\begin{aligned}
P_{\text{SN}} &= \frac{C_{\text{H I}}^2}{V} \sum_i (M_{\text{H I}}^i)^2 \\
&= \frac{\bar{T}_{\text{H I}}^2 V^2}{V} \sum_i (M_{\text{H I}}^i)^2 / \left(\sum_i M_{\text{H I}}^i \right)^2 \\
&= \bar{T}_{\text{H I}}^2 V \sum_i (M_{\text{H I}}^i)^2 / \left(\sum_i M_{\text{H I}}^i \right)^2.
\end{aligned} \tag{A14}$$

In other words, the shot noise power spectrum will then depend on the average H I temperature in a given cosmological volume, V , and the total H I mass in said volume. To calculate the shot noise, it is sufficient to know the masses of the galaxies in the cosmological volume, as the average H I temperature can also be computed from this.

Lastly, it is easy to see that in the case of all the galaxies having the same H I mass, the shot noise reduces to

$$\begin{aligned}
P_{\text{SN}} &= \bar{T}_{\text{H I}}^2 V \frac{N_{\text{g}}}{N_{\text{g}}^2} \\
&= \bar{T}_{\text{H I}}^2 \frac{V}{N_{\text{g}}} \\
&= \frac{\bar{T}_{\text{H I}}^2}{\bar{n}_{\text{g}}},
\end{aligned} \tag{A15}$$

which is a close analogue to the shot noise found in the galaxy power

spectrum, P_g . In that case, the shot noise is usually obtained by dividing A15 by T^2 , resulting in $P_{\text{SN}, g}(\mathbf{k}) \sim 1/\bar{n}_{\text{g}}$.

This paper has been typeset from a $\text{\TeX}/\text{\LaTeX}$ file prepared by the author.